AEROSPACE REPORT NO.
ATR-81(8454)-3

Simulation of the Magnetic Structure of the Inner Heliosphere by Means of a Non-Spherical Source Surface

Prepared by
R. H. LEVINE
Harvard-Smithsonian Center for Astrophysics
Cambridge, Massachusetts 02138

and

M. SCHULZ and E. N. FRAZIER
Space Sciences Laboratory
Laboratory Operations
The Aerospace Corporation

2 January 1981

Laboratory Operations
THE AEROSPACE CORPORATION

LABORATORY OPERATIONS

The Laboratory Operations of The Aerospace Corporation is conducting experimental and theoretical investigations necessary for the evaluation and application of scientific advances to new military concepts and systems Versatility and flexibility have been developed to a high degree by the laboratory personnel in dealing with the many problems encountered in the nation's rapidly developing space and missile systems Expertise in the latest scientific developments is vital to the accomplishment of tasks related to these problems The laboratories that contribute to this research are

Aerophysics Laboratory Launch and reentry aerodynamics, heat transfer, reentry physics, chemical kinetics, structural mechanics, flight dynamics, atmospheric pollution, and high-power gas lasers.

Chemistry and Physics Laboratory Atmospheric reactions and atmospheric optics, chemical reactions in polluted atmospheres, chemical reactions of excited species in rocket plumes, chemical thermodynamics, plasma and laser-induced reactions, laser chemistry, propulsion chemistry, space vacuum and radiation effects on materials, lubrication and surface phenomena, photosensitive materials and sensors, high precision laser ranging, and the application of physics and chemistry to problems of law enforcement and biomedicine

Electronics Research Laboratory Electromagnetic theory, devices, and propagation phenomena, including plasma electromagnetics, quantum electronics, lasers, and electro-optics, communication sciences, applied electronics, semiconducting, superconducting, and crystal device physics, optical and acoustical imaging, atmospheric pollution, millimeter wave and far-infrared technology

Materials Sciences Laboratory Development of new materials, metal matrix composites and new forms of carbon, test and evaluation of graphite and ceramics in reentry, spacecraft materials and electronic components in nuclear weapons environment, application of fracture mechanics to stress corrosion and fatigue-induced fractures in structural metals

Space Sciences Laboratory Atmospheric and ionospheric physics, radiation from the atmosphere, density and composition of the atmosphere, aurorae and airglow, magnetospheric physics, cosmic rays, generation and propagation of plasma waves in the magnetosphere, solar physics, studies of solar magnetic fields, space astronomy, x-ray astronomy, the effects of nuclear explosions, magnetic storms, and solar activity on the earth's atmosphere, ionosphere, and magnetosphere, the effects of optical, electromagnetic, and particulate radiations in space on space systems

THE AEROSPACE CORPORATION
El Segundo, California

. . .

Aerospace Report No.
ATR-81(8454)-3

SIMULATION OF THE MAGNETIC STRUCTURE OF THE INNER HELIOSPHERE BY MEANS OF A NON-SPHERICAL SOURCE SURFACE

Prepared by

R. H. Levine
Harvard-Smithsonian Center for Astrophysics
Cambridge, Massachusetts 02138

M. Schulz and E. N. Frazier
Space Sciences Laboratory
Laboratory Operations
The Aerospace Corporation

2 January 1981

Laboratory Operations
THE AEROSPACE CORPORATION
El Segundo, Calif. 90245

This Page Intentionally Left Blank

Aerospace Report No.
ATR-81(8454)-3

SIMULATION OF THE MAGNETIC STRUCTURE OF THE INNER HELIOSPHERE BY MEANS OF A NON-SPHERICAL SOURCE SURFACE

Prepared

E. N. Frazier for RHL
R. H. Levine
Harvard-Smithsonian Center for Astrophysics

Michael Schulz
M. Schulz
The Aerospace Corporation

E. N. Frazier
E. N. Frazier
Space Sciences Laboratory

Approved

J. B. Blake
J. B. Blake, Head
Space Particles and Fields Department

C. J. Rice
C. J. Rice, Head
Astrophysics and Remote Sensing Department

G. A. Paulikas
G. A. Paulikas, Director
Space Sciences Laboratory

This Page Intentionally Left Blank

ABSTRACT

In this work we implement a new method for mapping the Sun's magnetic field B from the photosphere through the corona and interplanetary space. The method entails the derivation of B from a scalar potential within a "current-free" annular volume bounded inside by the photosphere and outside by a prescribed non-spherical "source surface" to which B is made (as nearly as possible) perpendicular. As usual we obtain the potential for the part of B that arises from currents inside the Sun by fitting an expansion to the observed line-of-sight component of B at the photosphere. The new aspect of our work is that we introduce a second least-squares fit to obtain the part of B that arises from currents outside the source surface. We do this by minimizing the mean-square tangential component of B over the source surface. This latter prescription allows a nearly arbitrary specification of the source surface, and no particular symmetry properties need be invoked for it. We have chosen as our prescription of the source surface one that reasonably simulates the expected physical consequences of coronal MHD effects. The magnetic field exterior to the source surface is made perpendicular to the source surface and is mapped throughout the heliosphere by means of a geometrical construction that appropriately generalizes the Parker spiral. Detailed comparisons have been made between this new model and observed coronal and interplanetary structures. The equatorward inclination of coronal helmet streamers is modeled much better with a non-spherical source surface than with a spherical one. There is clear evidence, however, that observational data underestimate the strength of photospheric polar magnetic fields. Neutral lines on the source surface (*i.e.*, contours on which the normal component of B vanishes) generate heliospheric current sheets outside the source surface. In the particular case studied, two separate current sheets existed and were carried by the solar wind from the source surface to the boundary of the heliosphere. The result was a four-sector magnetic configuration near the ecliptic at 1AU, and the observations were in good agreement with this prediction of the model.

ACKNOWLEDGMENTS

We would like to thank Dr. R. Munro for assistance in the interpretation of HAO Skylab coronagraph data. This work was partially supported by the U.S. National Aeronautics and Space Administration (NASA) under contract NAS5-3949 with Harvard University and under contract NAS8-33376 with The Aerospace Corporation. Some of the computing resources used were provided by the National Center for Atmospheric Research (NCAR), which is sponsored by the U.S. National Science Foundation (NSF).

CONTENTS

This Page Intentionally Left Blank

FIGURES

1. Introduction

In this paper we develop and implement a significant new tool for constructing models of the coronal and interplanetary magnetic field from observations of the photospheric magnetic field. This tool, the non-spherical source surface, represents a significant improvement over previous models of solar magnetic field structure and is suitable for the study of the interplanetary magnetic field and its solar origin.

The study of the global magnetic configuration of the solar corona based on theoretical extrapolations of photospheric field measurements began with the work of Altschuler and Newkirk (1969) and Schatten *et al.* (1969). Both of these groups used the approach of solving Laplace's equation in an annular volume outside the photosphere in terms of a spherical harmonic expansion with coefficients of the harmonic functions depending on the measured magnetic field during an entire solar rotation. The neglect of coronal currents, necessary to obtain a unique solution in simple closed form, has proven acceptable in most cases (Levine and Altschuler, 1974; Poletto *et al.*, 1975). A harmonic expansion filling all space outside the photosphere would result in magnetic field lines that always return to the sun. This would not be an acceptable physical approximation to solar conditions because the solar wind plasma distorts the outer corona, creating "open" configurations consisting of field lines that begin on the sun but do not return. To overcome this difficulty, both Altschuler and Newkirk (1969) and Schatten *et al.* (1969) independently introduced a spherical outer boundary concentric with the solar surface. The scalar potential between the photosphere and this "source surface" was specified mathematically in such a way as to make the coronal field purely radial at the source surface itself. The field exterior to the source surface was constructed in accordance with the usual Parker (1958) spiral. The mathematical implementation of this concept was not difficult. It resulted in a modeling capability that accounted at least qualitatively for the effects of the solar wind on coronal

magnetic fields. Along with improvements in observational accuracy and resolution, improvements in both accuracy and efficiency in the modeling technique based on a spherical source surface have been achieved in recent years (Altschuler *et al.*, 1976; Adams and Pneuman, 1977; Riesebieter and Neubauer, 1979).

Applications of potential field models with spherical source surfaces have included studies of coronal structure at eclipse (Schatten, 1968; Altschuler and Newkirk, 1969; Smith and Schatten, 1970), coronal currents (Levine and Altschuler, 1974; Howard *et al.*, 1980), interplanetary magnetic fields (Schatten *et al.*, 1969; Levine *et al.*, 1977; Levine, 1978; Burlaga *et al.*, 1978), radio and MHD wave propagation in the corona (Uchida *et al.*, 1973; Smerd and Dulk, 1971; Jackson and Levine, 1980), and coronal holes and other sources of open magnetic fields (Levine, 1977; Svestka *et al.*, 1977). The success of these applications has been varied. The basic structure of coronal holes and the position/polarization of type III radio bursts, for example, are very well represented. However, the accuracy of the method is clearly less favorable in cases for which the exact structure of the outer corona near the source surface is important, as in the study of coronal structure at eclipse, the boundaries of coronal holes, and the magnitude of the interplanetary magnetic field. These deficiencies are due at least in part to the shortcomings of the spherical source surface as a simulation of the MHD effects that cause the structure of the outer corona. Many important physical problems, such as the possibility of open field lines in active regions, the orientation of helmet streamers, the source of the magnetic flux in the ecliptic plane, and the topology and evolution of interplanetary current sheets could be investigated with more confidence if the structure of the outer corona could be simulated more accurately than the spherical source surface allows.

As a step in this direction, the concept of a non-spherical source surface was introduced by Schulz *et al.* (1978). This yielded a good solution for the case of a

magnetic dipole at the center of the sun. Applicability to solar problems was demonstrated by showing a close correspondence with the full MHD solution for a dipolar magnetic field having boundary conditions of temperature and density roughly appropriate to the sun (Pneuman and Kopp, 1971). This correspondence opens the possibility for application of the non-spherical source surface to more elaborate magnetic field configurations, *i.e.*, to cases for which an MHD solution is not feasible. In the present work we extend the concept of a non-spherical source surface to the case of an arbitrary photospheric magnetic field and a more flexible specification of the source surface. In addition, we show that the field may be extended into interplanetary space without difficulty, except from regions where the source surface is concave.

This Page Intentionally Left Blank

2. Calculation of the Coronal Magnetic Field Inside a Non-Spherical Source Surface

Following the work of Schulz *et al.* (1978), we will derive solutions for the coronal and interplanetary magnetic field by using a non-spherical source surface. The goal is to simulate, on a global scale, physical processes whose effects cannot be calculated in detail if we wish to retain the great advantage of using measured photospheric magnetic fields as the inner boundary condition. As usual, the source surface represents the outer boundary of a current-free region. The magnetic field inside the source surface is derived from a potential V that is expanded in spherical harmonics, as in the earlier work of Schatten *et al.* (1969) and Altschuler and Newkirk (1969). The magnetic field outside the source surface is based on a geometrical construction that properly generalizes the spiral-field concept of Parker (1958), and the normal component of B is made continuous at the source surface. Because our source surface is non-spherical, the magnetic field will not (in general) be radial at the source surface. The field outside the source surface will consequently be diverted somewhat toward the main interplanetary neutral sheet (Schulz *et al.*, 1978) and away from the magnetic poles of the sun. Such diversion does not occur with a spherical source surface because (in that case) the θ component of B is required to vanish at the source surface and beyond.

As is usual in source surface calculations, we assume that the corona is current-free within the source surface and derive B from a scalar potential of the form

$$V = R_\odot \sum_{n=0}^{N} \sum_{m=0}^{n} \left(\frac{R_\odot}{r}\right)^{n+1} P_n^m(\theta)\,(g_n^m \cos m\phi + h_n^m \sin m\phi)$$

$$+ R_0 \sum_{n=1}^{\bar{N}} \sum_{m=0}^{n} \left(\frac{r}{R_0}\right)^{n} P_n^m(\theta)\,(\bar{g}_n^m \cos m\phi + \bar{h}_n^m \sin m\phi)\,. \qquad (1)$$

where r, θ, and ϕ are the usual spherical coordinates and the $P_n^m(\theta)$ are associated Legendre functions. For the case of a spherical source surface as outer boundary one obtains V=0 at $r=R_0$ by setting

$$(\bar{g}_n^m, \bar{h}_n^m) = -\left(\frac{R_\odot}{R_0}\right)^{n+2} (g_n^m, h_n^m) \qquad (2)$$

in (1). Previous authors have sometimes used the symbol r_s to denote the constant R_0 in the case of a spherical source surface. We use instead the equation $r=r_s(\theta,\phi)$ to describe the configuration of our non-spherical source surface, whose mean radius $\langle r_s \rangle$ is held equal to the constant R_0 that appears in equation (1). In order to obtain a set of g_n^m and h_n^m from observations of the photosphere we tentatively adopt a spherical source surface of (constant) radius R_0 and use equation (2) to eliminate $\bar{g}_n^m$ and $\bar{h}_n^m$ from equation (1). This procedure leaves the g_n^m and h_n^m as the only remaining parameters to be adjusted.

Observations provide values of the line of sight field B_ℓ^{obs} at $r=R_\odot$. The above harmonic expansion yields an algebraic expression for the line of sight field $B_\ell = B_r \sin(\theta+\beta) + B_\theta \cos(\theta+\beta)$, where $\mathbf{B}=-\nabla V$ is obtained from equation (1) and β is the average solar B-angle during the time of the magnetic observations (*i.e.*, β is the heliographic latitude of the observer). By requiring that the integral of $[B_\ell^{obs} - (B_r \sin(\theta+\beta) + B_\theta \cos(\theta+\beta))]^2$ over the photosphere be a minimum with respect to variation of the coefficients g_n^m and h_n^m, a set of simultaneous linear equations for the coefficients can be obtained. If N is the largest principal index of the coefficients g_n^m and h_n^m to be calculated, there are $(N+1)^2$ equations and $(N+1)^2$ unknowns, forming a $(N+1)^2 \times (N+1)^2$ matrix problem. However, symmetry properties of the harmonic functions decouple the equations into blocks of N-m+1 simultaneous equations, reducing the largest number of independent equations which must be solved at one time to N+1 (Altschuler *et al.*, 1976). This makes it practical to solve for coefficients g_n^m and h_n^m with values of N whose corresponding

harmonic functions have a structure matching the scale of synoptic magnetic observations (*e.g.*, up to N=90 for synoptic data of approximately 1° resolution).

For the case of a non-spherical source surface, we recompute the $\bar{g}_n^m$ and $\bar{h}_n^m$ as an independent set of coefficients whose values depend not only on the photospheric field distribution and mean radius of the source surface, but also on the shape and orientation of the source surface. The boundary condition at the non-spherical source surface should be that the field is perpendicular to the surface. However, for a non-spherical source surface with V given by equation (1) this boundary condition cannot be satisfied exactly over the entire surface; it can be satisfied only in the least-squares sense. Therefore, a second least-squares fit of the $\bar{g}_n^m$ and $\bar{h}_n^m$ to the outer boundary condition is required. This second least-squares fit is the primary difference between the solution for a spherical source surface and that for a non-spherical source surface.

The components of the magnetic field in the region between the solar surface and the non-spherical source surface are

$$B_r = \sum_{n=0}^{N} \sum_{m=0}^{n} (n+1) \left(\frac{R_\odot}{r}\right)^{n+2} P_n^m(\theta) \left(g_n^m \cos m\phi + h_n^m \sin m\phi\right)$$

$$- \sum_{n=1}^{\bar{N}} \sum_{m=0}^{n} n \left(\frac{r}{R_0}\right)^{n-1} P_n^m(\theta) \left(\bar{g}_n^m \cos m\phi + \bar{h}_n^m \sin m\phi\right) \qquad (3a)$$

$$B_\theta = -\sum_{n=0}^{N} \sum_{m=0}^{n} \left(\frac{R_\odot}{r}\right)^{n+2} \frac{dP_n^m(\theta)}{d\theta} \left(g_n^m \cos m\phi + h_n^m \sin m\phi\right)$$

$$- \sum_{n=1}^{\bar{N}} \sum_{m=0}^{n} \left(\frac{r}{R_0}\right)^{n-1} \frac{dP_n^m(\theta)}{d\theta} \left(\bar{g}_n^m \cos m\phi + \bar{h}_n^m \sin m\phi\right) \qquad (3b)$$

$$B_\phi = \sum_{n=0}^{N}\sum_{m=0}^{n}\left(\frac{R_0}{r}\right)^{n+2} m\,\frac{P_n^m(\theta)}{\sin\theta}\,(g_n^m \sin m\phi - h_n^m \cos m\phi)$$

(3c)

$$+ \sum_{n=1}^{\bar{N}}\sum_{m=0}^{n}\left(\frac{r}{R_0}\right)^{n-1} m\,\frac{P_n^m(\theta)}{\sin\theta}\,(\bar{g}_n^m \sin m\phi - \bar{h}_n^m \cos m\phi)\,.$$

Notice that we have identified a separate value $\bar{N}\,(\neq N)$ for the maximum principal index of the coefficients $\bar{g}_n^m$ and $\bar{h}_n^m$. The reason for this will be made apparent below.

We let the non-spherical source surface be defined by $r_s(\theta,\phi)$ with $\hat{n}(\theta,\phi)$ the unit normal vector field on the source surface and we let $R_0=\langle r_s\rangle$. We further assume that the coefficients g_n^m and h_n^m are known. Because we cannot make the field be normal to the source surface at each point, we instead minimize the mean-square tangential component of **B** at the source surface. Defining the tangential component of the magnetic field at the source surface by

$$B_t^2 = |\,\hat{n}\times\mathbf{B}\,|^2 = B^2 - (\hat{n}\cdot\mathbf{B})^2\,, \tag{4}$$

we wish to minimize

$$\sigma \equiv \int B_t^2\,dA = \int_0^{2\pi}\int_0^{\pi} B_t^2\,\frac{r^2\sin\theta}{|\hat{n}\cdot\hat{r}\,|}\,d\theta\,d\phi \tag{5}$$

with respect to each of the $\bar{g}_n^m$ and $\bar{h}_n^m$. Setting $\partial\sigma/\partial\bar{g}_{n'}^{m'}=0$, we obtain (see Appendix for details) the equation

$$\sum_{n=1}^{\bar{N}}\sum_{m=0}^{n}\bar{g}_n^m\int_0^{2\pi}\int_0^{\pi}\left(\left\{\nabla\left[\left(\frac{r}{R_0}\right)^n P_n^m(\theta)\cos m\phi\right]\right\}\cdot\left\{\nabla\left[\left(\frac{r}{R_0}\right)^{n'} P_{n'}^{m'}(\theta)\cos m'\phi\right]\right\}\right.$$

$$\left.-\left\{\hat{n}\cdot\nabla\left[\left(\frac{r}{R_0}\right)^n P_n^m(\theta)\cos m\phi\right]\right\}\left\{\hat{n}\cdot\nabla\left[\left(\frac{r}{R_0}\right)^{n'} P_{n'}^{m'}(\theta)\cos m'\phi\right]\right\}\right)\frac{r^2\sin\theta}{|\hat{n}\cdot\hat{r}\,|}\,d\theta\,d\phi$$

$$+\sum_{n=1}^{\bar{N}}\sum_{m=0}^{n}\bar{h}_n^m\int_0^{2\pi}\int_0^{\pi}\left(\left\{\nabla\left[\left(\frac{r}{R_0}\right)^n P_n^m(\theta)\sin m\phi\right]\right\}\cdot\left\{\nabla\left[\left(\frac{r}{R_0}\right)^{n'} P_{n'}^{m'}(\theta)\cos m'\phi\right]\right\}\right.$$

$$\left.-\left\{\hat{n}\cdot\nabla\left[\left(\frac{r}{R_0}\right)^n P_n^m(\theta)\sin m\phi\right]\right\}\left\{\hat{n}\cdot\nabla\left[\left(\frac{r}{R_0}\right)^{n'} P_{n'}^{m'}(\theta)\cos m'\phi\right]\right\}\right)\frac{r^2\sin\theta}{|\hat{n}\cdot\hat{r}|}\,d\theta\,d\phi$$

$$=\frac{R_\odot}{R_0}\sum_{n''=1}^{N}\sum_{m''=0}^{n''} \tag{6}$$

$$g_{n''}^{m''}\int_0^{2\pi}\int_0^{\pi}\left(\left\{\hat{n}\cdot\nabla\left[\left(\frac{R_\odot}{r}\right)^{n''+1} P_{n''}^{m''}(\theta)\cos m''\phi\right]\right\}\left\{\hat{n}\cdot\nabla\left[\left(\frac{r}{R_0}\right)^{n'} P_{n'}^{m'}(\theta)\cos m'\phi\right]\right\}\right.$$

$$\left.-\left\{\nabla\left[\left(\frac{R_\odot}{r}\right)^{n''+1} P_{n''}^{m''}(\theta)\cos m''\phi\right]\right\}\cdot\left\{\nabla\left[\left(\frac{r}{R_0}\right)^{n'} P_{n'}^{m'}(\theta)\cos m'\phi\right]\right\}\right)\frac{r^2\sin\theta}{|\hat{n}\cdot\hat{r}|}\,d\theta\,d\phi$$

$$+\frac{R_\odot}{R_0}\sum_{n''=1}^{N}\sum_{m''=0}^{n'}$$

$$h_{n''}^{m''}\int_0^{2\pi}\int_0^{\pi}\left(\left\{\hat{n}\cdot\nabla\left[\left(\frac{R_\odot}{r}\right)^{n''+1} P_{n''}^{m''}(\theta)\sin m''\phi\right]\right\}\left\{\hat{n}\cdot\nabla\left[\left(\frac{r}{R_0}\right)^{n'} P_{n'}^{m'}(\theta)\cos m'\phi\right]\right\}\right.$$

$$\left.-\left\{\nabla\left[\left(\frac{R_\odot}{r}\right)^{n''+1} P_{n''}^{m''}(\theta)\sin m''\phi\right]\right\}\cdot\left\{\nabla\left[\left(\frac{r}{R_0}\right)^{n'} P_{n'}^{m'}(\theta)\cos m'\phi\right]\right\}\right)\frac{r^2\sin\theta}{|\hat{n}\cdot\hat{r}|}\,d\theta\,d\phi$$

A similar expression is obtained from the condition $\partial\sigma/\partial\bar{h}_{n'}^{m'}=0$, except that the $\cos m'\phi$ terms in equation (6) are replaced by $\sin m'\phi$.

Together, equation (6) and its analog represent $\bar{N}(\bar{N}+2)$ simultaneous linear equations for the unknowns $\bar{g}_n^m$ and $\bar{h}_n^m$. There is one equation for each n' for $m'=0$, and there are two equations for each combination of indices

$(n'; m')=(1, 2, \ldots, \bar{N}; 1, 2, \ldots, n')$. The coefficients of the unknowns $\bar{g}_n^m$ and $\bar{h}_n^m$ are the integrals on the left hand side of equation (6) and its analog. These form a matrix with $\bar{N}(\bar{N}+2) \times \bar{N}(\bar{N}+2)$ elements (see Appendix for details). The right hand side of each equation consists of the integrals on the right hand side of equation (6) and its analog. These form a column vector of $\bar{N}(\bar{N}+2)$ elements. Because any continuous $r_s(\theta,\phi)$ with $n_r \equiv \hat{n} \cdot \hat{r} \neq 0$ everywhere can be specified as the source surface, it is clear that no general symmetry exists in equation (6) which reduces the number of independent equations in all cases. The harmonic functions are not mutually orthogonal over a non-spherical source surface because both r and $\hat{n} \cdot \hat{r}$ depend on θ and ϕ in the general case. There is not even enough symmetry in general to decouple the linear equations corresponding to distinct values of n or m. Thus the full $\bar{N}(\bar{N}+2) \times \bar{N}(\bar{N}+2)$ matrix must be calculated and solved to obtain a solution for a set of $\bar{g}_n^m$ and $\bar{h}_n^m$, and it is computationally prohibitive to set $\bar{N}=N$ We can possibly afford to take N=90 in deducing the g_n^m and h_n^m from line-of-sight data, but we cannot afford to take $\bar{N} \gtrsim 15$ in deducing the $\bar{g}_n^m$ and $\bar{h}_n^m$ appropriate to a non-spherical source surface. The former operation requires us to compute $\sim N^3/3$ matrix elements (*i.e.*, 2.4×10^5 elements for N=90), while the latter operation requires us to compute $\bar{N}^4$ matrix elements (*i.e.*, 4×10^4 elements for $\bar{N}=14$ and 6.4×10^7 elements for $\bar{N}=90$).

As a compromise between thrift and resolution, we typically take N=25 (with an integration grid of 60 latitude zones by 120 longitude sectors) and $\bar{N}=6$ with a grid of 18 x 36). Further discussions of this solution are given in the Appendix. Calculating the matrix elements (which requires the most computation time) and solving the system of linear equations (which uses less than 5% of the computation time) typically takes 20 times longer for the $\bar{g}_n^m$ and $\bar{h}_n^m$ up to $\bar{N}=6$ than for the g_n^m and h_n^m up to N=25 (even with the finer integration grid used at the photosphere). This ratio is insensitive to the computing power applied, being essentially invariant between a PDP 11/60 minicomputer and a CRAY-1. Calculation of such a set of $\bar{g}_n^m$

and $\bar{h}_n^m$ can be completed in approximately one hour on a PDP 11/60 or 7 seconds on a CRAY-1. This time increases approximately as $2\bar{N}^4$. For example, a solution for $\bar{N}$=14 (224 x 224 matrix) requires 7 minutes on a CRAY-1.

Because the contribution of the $\bar{g}_n^m$ and $\bar{h}_n^m$ terms in equations (3) is non-zero at $r=R_\odot$, the full solution derived above will not satisfy quite the same photospheric boundary condition that the solution for a spherical source surface satisfies. A fully self-consistent model that satisfies both boundary conditions at once would seem to require a simultaneous least-squares solution for all the coefficients when the source surface is non-spherical. In the present application of our model, however, the configuration of the source surface itself depends on the g_n^m and h_n^m (see below). Thus, any simultaneous fit for the g_n^m, h_n^m, $\bar{g}_n^m$, and $\bar{h}_n^m$ would be highly nonlinear in the g_n^m and h_n^m. The implementation of such a scheme would be computationally prohibitive. However, we do not expect the deviations of the $\bar{q}_r^m$ and $\bar{h}_n^m$ from (2) to be so large as to invalidate our determination (described above) of the g_n^m and h_n^m from line-of-sight data at the photosphere. Our confidence rests on the fact that the second line of equation (1) contributes little to the field at $r=R_\odot$ in any event, *i.e.*, about one part in $(R_0/R_\odot)^{2n+1}$ for harmonic number n. Thus, in the numerical implementation of equation (6) and its analog, the coefficients g_n^m and h_n^m which are used are those defined by the measured photospheric field distribution but with a spherical source surface at $r=\langle r_s \rangle$. This use of a spherical source surface to determine the "photospheric" coefficients g_n^m and h_n^m is easily implemented, since it modifies but slightly the algebraic form of B_ℓ from that used by Altschuler *et al.* (1976). The values of g_n^m and h_n^m thus determined are also used in the calculation of magnetic field components by means of (3).

This Page Intentionally Left Blank

3. Specification of the Non-Spherical Source Surface

The formulation of Section 2 is applicable to any non-spherical source surface, subject only to the restrictions that $r_s(\theta,\phi)$ is continuous and that $n_r \equiv \hat{n}\cdot\hat{r} \neq 0$ everywhere. For practical application it is necessary to choose a definition of the non-spherical source surface that is both physically motivated and computationally acceptable. In order to distinguish clearly between the physical prescription of the source surface and its application to the solution for **B**, we define a general analytic function $F(r,\theta,\phi)$ and require the source surface to be a surface of constant F. We have chosen an initial definition of F which is based on physical expectations and which has particular computational advantages. We expect that refinements will be made in the physical prescription used to choose a source surface as the usefulness of this method is explored.

The purpose of a non-spherical source surface is to simulate the implications of having a non-radial solar wind at and beyond the outer boundary of the current free region. The non-radial solar wind is a fully expected consequence of MHD (Pneuman and Kopp, 1971). Schulz *et al.* (1978) suggested that the magnetic field

$$\tilde{\mathbf{B}} \equiv -R_\odot \nabla \sum_{n=1}^{N} \sum_{m=0}^{n} \left(\frac{R_\odot}{r}\right)^{n+1} (g_n^m \cos m\phi + h_n^m \sin m\phi) P_n^m(\theta) \qquad (7)$$

derived solely from internal sources, *i.e.*, from the first line of (1), be considered as the basis for specifying the source surface. By choosing $F=\tilde{B}^2$, Schulz *et al.* (1978) specified the source surface as an isogauss of (7), *i.e.*, as a surface of constant $|\tilde{\mathbf{B}}|$, and thereby obtained a rather good simulation of the Pneuman-Kopp MHD solution for the case of an internal solar dipole.

For more realistic cases, however, we have found too often that an isogauss of (7) is not a convex surface. In other words, it happens too often that the source surface specified by Schulz *et al.* (1978) is indented in places. This

condition seriously complicates the geometrical construction of B outside the source surface, because it permits solar-wind streams from different parts of the source surface to intersect. Intersecting streams may well be present in the real solar wind, but they impose mathematical difficulties that we wish to avoid in the present model. Accordingly, we have re-opened the question of how to specify an optimal source surface and have discovered a suitable compromise between the spherical source surface and the isogauss of $|\tilde{B}|$.

Our new procedure is based on a more general specification of F, namely

$$F = \alpha \tilde{B}^2 + (1-\alpha)\, \tilde{B}_1^2 \frac{\langle r_1^{\nu} \rangle}{r^{\nu}}, \tag{8}$$

in which α and ν are parameters to be chosen. We have fixed $\nu=4$ for convenience The effect of choosing the parameter $\alpha<1$ is to generate a surface of constant F that is smoother than an isogauss of $\tilde{B}$, but has the same average radius. Thus the case $\alpha=0$ produces a spherical source surface of radius R_0, while the case $\alpha=1$ produces a source surface that is an isogauss of $\tilde{B}$ with average radius $\langle r_s \rangle = R_0$. The constants $\tilde{B}_1^2$ and $\langle r_1^{\nu} \rangle$ are determined in an initial step by setting $\alpha=1$ in (8) and finding the values of $\tilde{B}$ and $\langle r_1^{\nu} \rangle$ that correspond to an isogauss of mean radius $\langle r_s \rangle = R_0$. Thereafter we generate surfaces of constant F for any desired values of $\alpha<1$ by holding $\langle r_s \rangle = R_0$, but we do not recalculate the constants $\tilde{B}_1^2$ and $\langle r_1^{\nu} \rangle$

The outward normal to the source surface is the unit vector in the direction of $-\nabla F$, *i.e.*, the unit vector $\hat{n} = -\nabla F / |\nabla F|$. Because F is expressed analytically by equation (8) with the help of equation (7), we can also express $\hat{n}$ analytically, and there is no need for numerical differentiation to calculate $\hat{n}$.

Some implications of selecting a value of α other than $\alpha=0$ (Altschuler and Newkirk, 1969) or $\alpha=1$ (Schulz *et al.*, 1978) are illustrated in Figures 1-4. Figure 1 shows a longitudinal section of the source surface corresponding to a photospheric

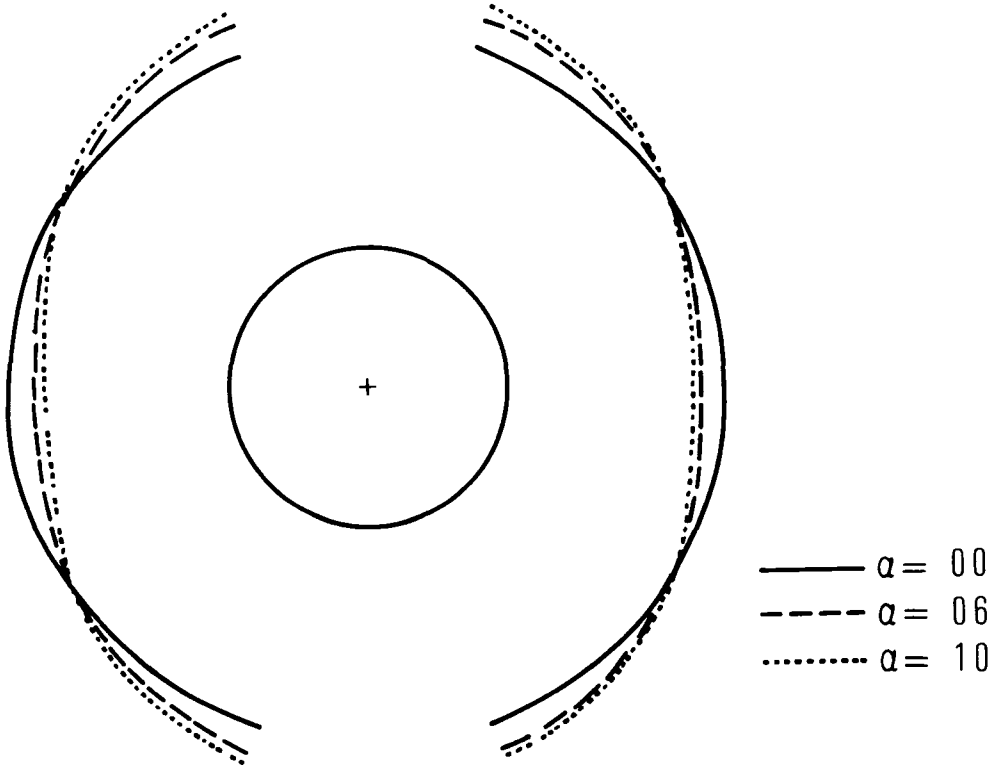

Figure 1 Longitudinal section of the source surface corresponding to a photospheric dipole for three different values of α. The average radius of each surface is 2.58 $R_{\odot}$.

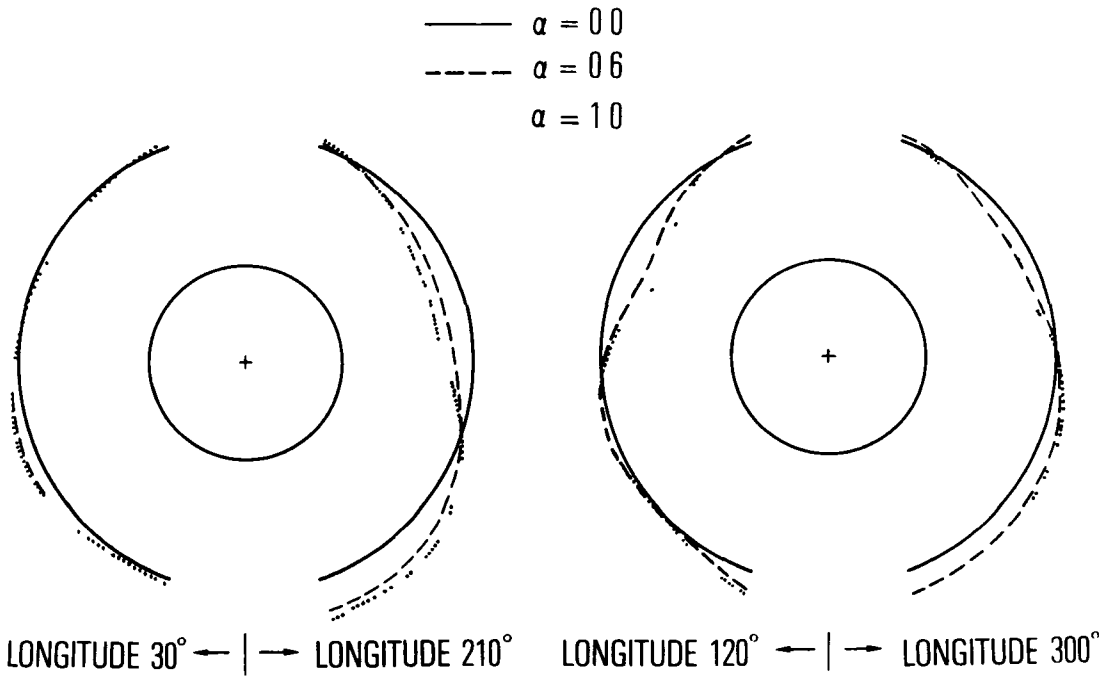

Figure 2 **Longitudinal sections of the source surface calculated from the measured photospheric magnetic field for Carrington rotation 1602 for three different values of α. Where the α=0.6 surface is not shown, it essentially coincides with the α=1 surface. The average radius of each surface is 2.3 $R_{\odot}$.**

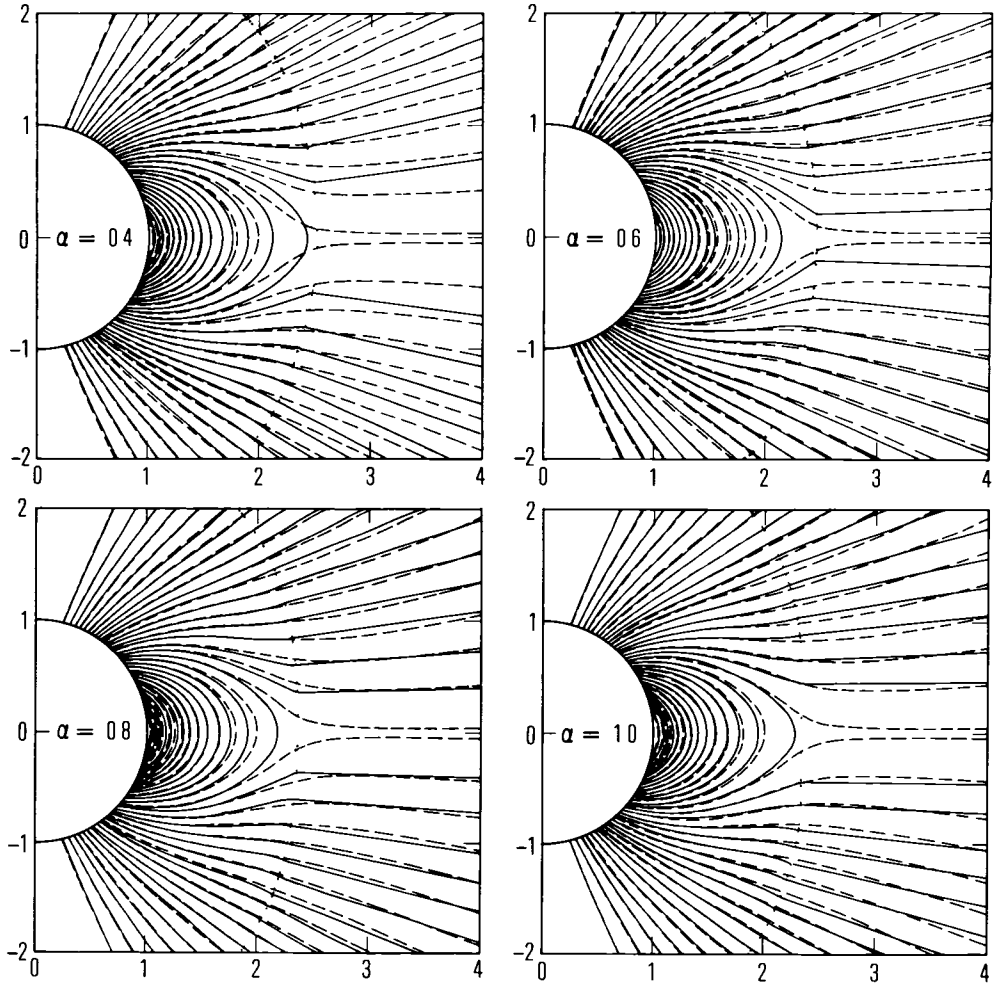

Figure 3 Comparison of magnetic field lines calculated by the present model (solid lines) with field lines calculated by the MHD model (dashed lines) of Pneuman and Kopp (1971) for different values of α. The footpoints of our computed field lines were chosen to match those of the Pneuman-Kopp field lines. The location of the source surface is indicated by dotted lines.

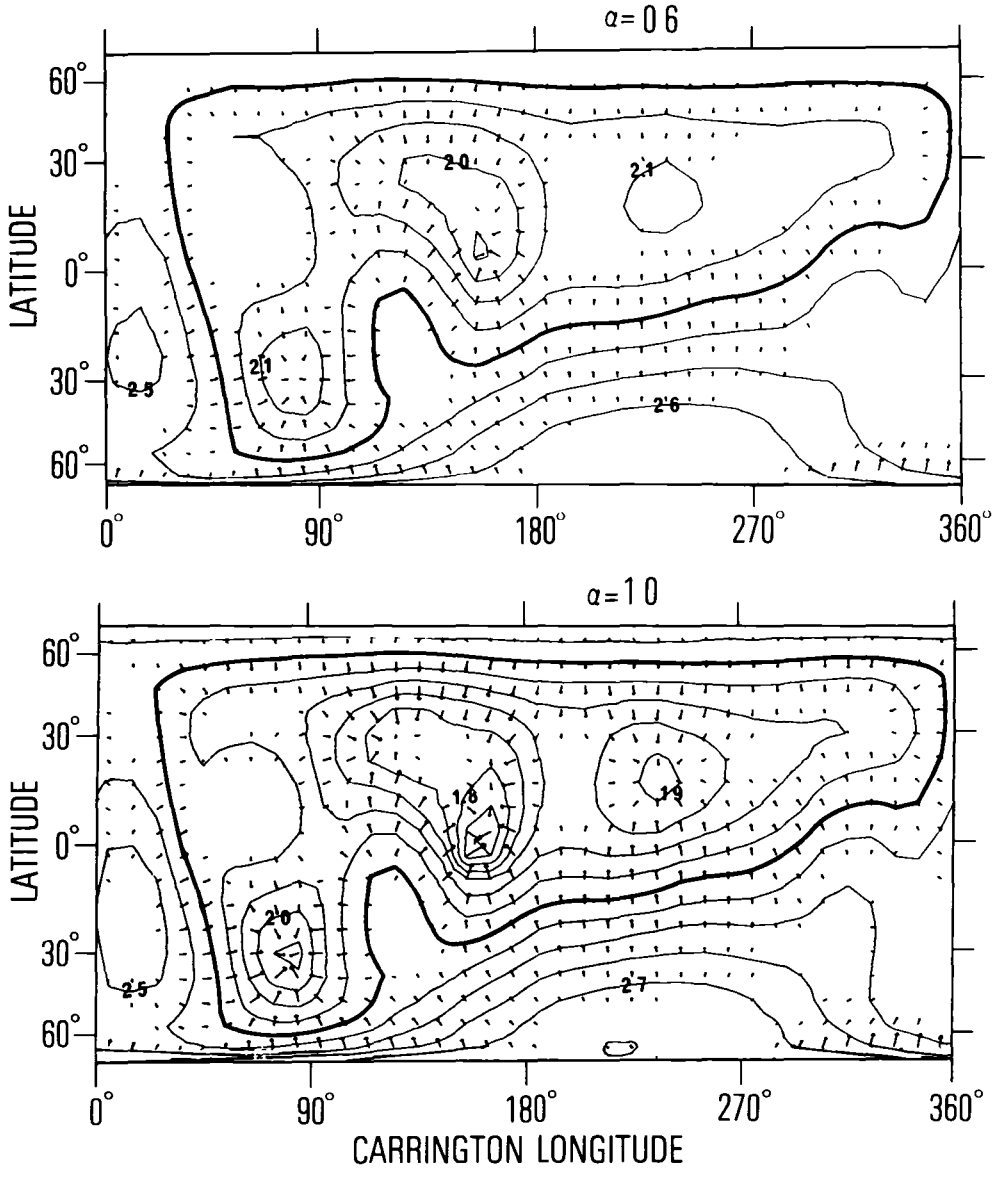

Figure 4 Contours of constant r_s for Carrington rotation 1602, with two different values of α, in synoptic chart format. Contour lines are shown at intervals of 0.1 $R_\odot$; the contour at $r_s=\langle r_s \rangle=2.3\ R_\odot$ is thickened. The arrows are projections of the unit normal vector onto the unit sphere.

dipole ($g_1^0 \neq 0$) for each of several values of α. The value of $\langle r_s \rangle$ is held approximately equal to 2.58 $R_\odot$ in each case. Figure 2 shows certain longitudinal sections of the source surface corresponding to the g_n^m and h_n^m deduced from the measured line-of-sight field at the photosphere for Carrington rotation 1602. The values of α are the same in Figure 2 as in Figure 1, but the value of $\langle r_s \rangle$ is held equal to 2.3 $R_\odot$ in Figure 2. We see that a choice of α somewhat less than unity can often eliminate concave areas (indentations) that occur on the source surface for α=1.

For the present, we assume that the optimal value of α in general can be determined by reexamining the case of a photospheric dipole. Thus, we have constructed a source surface of mean radius $\langle r_s \rangle$=2.58 $R_\odot$ for each of several values of α and have carried out the other steps described above for the case in which g_1^0 is the only nonvanishing coefficient among the g_n^m and h_n^m. All the coefficients $\bar{g}_n^m$ and $\bar{h}_n^m$ that should vanish in this case (*i.e.*, all except $\bar{g}_1^0$, $\bar{g}_3^0$, and $\bar{g}_5^0$ for $\bar{N}$=6) indeed turned out to be very small. We computed B from (3) and plotted certain of the field lines on a meridional plane. The results are shown in Figure 3 as solid curves. The dashed curves in Figure 3 are the field lines obtained by Pneuman and Kopp (1971) in their MHD study of the photospheric-dipole case. Our field lines were chosen to have the same heliographic latitudes at r=$R_\odot$ as the Pneuman-Kopp field lines.

The choice α=1 in Figure 3 corresponds to the solution of Schulz *et al.* (1978), although our Figure 3d differs somewhat from their Figure 2. Such minor differences should be expected, since (a) our $\langle r_s \rangle$=2.58 $R_\odot$ exceeds their $\langle r_s \rangle$=2.547 $R_\odot$ by about 1%, (b) our integration grid in equation (6) is necessarily coarser than theirs, (c) our $\bar{N}$=6 is necessarily smaller their $\bar{N}$=15, and (d) our procedure for tracing field lines differs somewhat from theirs. Regardless of these differences, it is clear that the choice of α=1 implicit in the work of Schulz *et al.* (1978) produced a good

simulation of the MHD results of Pneuman and Kopp (1971), whereas the adjustability of α in the present work offers the prospect of improved simulation. It is particularly important in this context to model well the asymptotic directions of the field lines, because one of our main motives for developing the non-spherical source surface has been to extend the model as accurately as possible throughout the heliosphere. It is clear from Figure 3 that the choice α=1 provides too much of an equatorial deflection of field lines from the radial direction outside the source surface, whereas the choice α=0.4 provides too little. The four panels of Figure 3 all show rather good agreement between our model and the MHD results inside the source surface (dotted curve) in each case. In selecting an optimal α, we do not rely heavily on comparative details in the vicinity of the cusped MHD field line. Our model is current-free within the source surface and so inherently produces a Y-type neutral line, whereas MHD produces a cusp-type neutral line (Sturrock and Smith, 1968; Pneuman and Kopp, 1971). Taking these various factors into account, we conclude from Figure 3 that a choice of α in the range 0.6-0.8 best simulates the MHD solution overall. We have seen from Figure 2 that this range of α tends to yield a convex source surface when used with photospheric data, as desired.

Although we will restrict our further examples to isogauss surfaces with α in the range 0.6-0.8 (*cf.* equation (8)), it should be remembered that this choice is based on comparison with an MHD solution that is azimuthally symmetric and represents an isothermal corona. Both of these restrictions are serious compromises with the known physics of the solar corona. Thus, it would not be surprising if further progress in simplified MHD models of the corona pointed the way to different ranges of α, or, more likely, to different ways of specifying a three-dimensional non-spherical source surface.

A global view of two of the source surfaces profiled in Figure 2 is given in synoptic chart format in Figure 4. Here the contours of constant heliocentric

distance on the source surface are incremented in steps of 0.1 $R_\odot$, and the contour $r=\langle r_s \rangle=2.3\,R_\odot$ is heavier than the others. The arrows represent projections of the unit normal vector $\hat{n}$ on the unit sphere, and so have lengths proportional to $(n_\theta^2 + n_\phi^2)^{1/2}$. The shorter projections thus correspond to the more nearly radial orientations of the unit normal. Concave areas are not readily identified in this format, but the presence of fewer contours for α=0.6 suggests that the source surface is more nearly spherical (as expected) for α=0.6 than for α=1. Centers of convergence (toward which the arrows point) do not necessarily indicate concave areas but do indicate regions above which |B| diminishes less rapidly than Parker (1958) suggests with heliocentric distance beyond the source surface. Centers from which arrows emanate identify regions above which |B| diminishes more rapidly with r than Parker (1958) suggests. The variation of B interior to the source surface enables open field lines to map the entire source surface onto a rather small fraction of the photosphere (Levine, 1977). Thus, the variation of |B| with r inside the corona must be considerably stronger than inverse-square on the average. Most coronal magnetic models possess this last property. Ours offers the further prospect of modeling the variation of |B|, and thus of flux-tube area as a function of r (Nerney and Suess, 1975; Suess *et al.*, 1977; Levine, 1978), all the way from the photosphere to the outer boundary of the heliosphere.

This Page Intentionally Left Blank

4. Coronal Magnetic Field Models Inside the Non-Spherical Source Surface

4.1 Accuracy of the Solution for $\bar{g}_n^m$ and $\bar{h}_n^m$

In Section 2 it was pointed out that the least-squares solution for the coefficients $\bar{g}_n^m$ and $\bar{h}_n^m$ for a non-spherical source surface will not, in general, satisfy the boundary condition $\mathbf{B} \times \hat{n} = 0$ exactly at all points on the source surface. In addition to accuracy in the above sense, we consider in this section the precision of the numerical procedures used to solve equation (6) for the coefficients $\bar{g}_n^m$ and $\bar{h}_n^m$. (The stability of the solution is discussed in the Appendix.)

The precision of the numerical solution of equation (6) can be checked by calculating coefficients in cases for which the answer is known by some independent means. One such case is a spherical source surface, which can be considered a degenerate case of equation (8) with $\alpha=0$. In this case the coefficients $\bar{g}_n^m$ and $\bar{h}_n^m$ are given exactly by equation (2). Our procedure entails the numerical computation of matrix elements over a finite integration grid, and so our results for $\bar{g}_n^m$ and $\bar{h}_n^m$ do not agree exactly with (2). However, calculation of $\bar{g}_n^m$ and $\bar{h}_n^m$ using equation (6) with a source surface given by $\alpha=0$ (*i.e.*, $r_s(\theta,\phi)=R_0$; $\hat{n}=\hat{r}$) satisfies equation (2) to within 0.1% in all cases that we have examined.

A more stringent test is the case of a photospheric dipole with a source surface that is an isogauss of $\tilde{B}$ (*i.e.*, $\alpha=1$). Schulz *et al.* (1978) calculated the coefficients $\bar{g}_n^0$ ($n=1, 3, 5, \ldots, \bar{N}$) for this case by obtaining a solution that assumed azimuthal and north-south symmetry and that specified $r_s(\theta,\phi)$ and $\hat{n}$ analytically. They obtained accurate numerical results for $\bar{g}_n^0/g_1^0$ (for various values of $\bar{N}$), and needed to solve at most $(\bar{N}+1)/2$ simultaneous linear equations for this case, because the symmetry of the problem required that $\bar{g}_n^m$ and $\bar{h}_n^m$ vanish unless $m=0$ and n is odd. Our present code does not constrain any of the

coefficients $\bar{g}_n^m$ or $\bar{h}_n^m$ in (1) to vanish. Numerical solution of equation (6) under the conditions discussed in Section 2 (r_s defined on a grid of 18×36 values; $\bar{N}$=6) gives agreement with the values of $\bar{g}_1^0$, $\bar{g}_3^0$, and $\bar{g}_5^0$ calculated by Schulz *et al.* (1978) to within 0.39% for $\bar{g}_1^0$, 2.60% for $\bar{g}_3^0$, and 3.74% for $\bar{g}_5^0$. The other coefficients should be zero for this dipole case. For $m \neq 0$ this is true in our numerical calculation by at least six orders of magnitude compared to $\bar{g}_1^0$. For m=0 the average of the absolute values of the coefficients $\bar{g}_2^0$, $\bar{g}_4^0$, and $\bar{g}_6^0$ is 0.56% of the average of the absolute values of the the three non-zero coefficients.

We have investigated separately the effects of increasing $\bar{N}$ and of doubling the number of source surface grid points in our numerical calculation. Each of these can improve the agreement with the results of Schulz *et al.* (1978), but there appears to be a limit to the agreement of the n=1, 3, and 5 coefficients at about one-half to one-third of the percentages given above. Moreover, with $\bar{N} \simeq 14$, the largest value tested in our numerical scheme, the agreement was not satisfactory for odd values of $n \gtrsim 9$. We conclude that, with the present numerical procedure, optimal solutions (in terms of overall agreement with the results of Schulz *et al.*, 1978) are obtained for $\bar{N}$=6 or 8 and an integration grid at least as fine as 18 x 36, and preferably 36 x 72. The increasing size of the fairly sparse matrix for larger $\bar{N}$ (*e.g.*, 224 x 224 for $\bar{N}$=14) seems to introduce numerical difficulties that adversely affect the convergence of the coefficients having higher values of n.

The minimization of σ for a non-spherical source surface does not (in general) cause σ (equation (5)) to vanish exactly, but it should cause the strong inequality $|\mathbf{B} \times \hat{\mathbf{n}}|^2 \ll (R_\odot/R_0)^6 [(g_1^0)^2 + (g_1^1)^2 + (h_1^1)^2]$ to hold over most of the source surface. Thus, we expect to find $\sigma \ll 4\pi (R_\odot{}^6/R_0{}^4) [(g_1^1)^2 + (g_1^1)^2 + (h_1^1)^2]$ for the optimal expansion coefficients $\bar{g}_n^m$ and $\bar{h}_n^m$, and we expect to find the integrand $|\mathbf{B} \times \hat{\mathbf{n}}|^2$ to be distributed like random noise over the source surface. Our

numerical results largely confirm these expectations. For the case of a photospheric dipole with α=0.8 (see Figure 3c) we found $\sigma=0.0175\times 4\pi(R_\odot{}^6/R_0{}^4)\,(g_1^0)^2$, with $|\mathbf{B}\times\hat{\mathbf{n}}|_s^2 < 0.087\,(R_\odot/R_0)^6\,(g_1^0)^2$ everywhere. However, because this special case was azimuthally symmetric, we found no variation of $|\mathbf{B}\times\hat{\mathbf{n}}|_s^2$ with longitude. Instead we found, as did Schulz *et al.* (1978), that contours of constant $|\mathbf{B}\times\hat{\mathbf{n}}|_s^2$ divided the source surface into latitudinal bands.

In more realistic cases, *e.g.*, for the g_n^m and h_n^m deduced from line-of-sight photospheric field data for Carrington rotation 1602, the azimuthal asymmetry of the source surface (see Figure 4, above) causes the distribution of $|\mathbf{B}\times\hat{\mathbf{n}}|_s^2$ to appear essentially disorganized with respect to θ and ϕ, as desired. Moreover, the values of σ turn out to be small, satisfying the inequalities proposed above. We have verified that the above inequalities are satisfied more strongly in all cases when the number of grid points on the source surface is doubled and (with somewhat less improvement) when larger $\bar{N}$ is used. Thus, we have good confidence in the utility of our model for application to actual coronal and photospheric data, as well as to idealizations of the sun's magnetic field.

4.2 Comparison with Coronal Data

We have chosen the Skylab ATM era as the best time period for comparison with coronal data because of the completeness of the data set. Because the most visible effect of incorporating a non-spherical (rather than spherical) source surface into coronal magnetic models is that the calculated helmet streamers now can be non-radial, we have selected the ATM coronagraph data as the most relevant ATM data for comparison with the model. In particular, the total eclipse of 30 June 1973 yields the best data for comparison because there are also ground-based photographs that show coronal structure down to $r=R_\odot$. Furthermore, there was

relatively little evolution of the sun's magnetic field during this time period (Levine, 1978).

The non-spherical source surface adopted for the eclipse time period is shown in Figure 5 in the same format as Figure 4. For the calculation of this surface and the coefficients g_n^m, h_n^m, $\bar{g}_n^m$ and $\bar{h}_n^m$ photospheric magnetic data from Carrington longitude 180° of rotation 1602 to longitude 180° of rotation 1603 were used. In calculating the non-spherical source surface we have been guided by the experience of the dipolar case (see Figure 3 above) to choose a value of α=0.8 in equation (8). The value of $\langle r_s \rangle$ was chosen to produce a source surface height that matched the tops of the helmet streamers visible at the 1973 eclipse. The average radius of the source surface in Figure 5 is 2.72 $R_\odot$ and the extrema are 1.92 $R_\odot$ and 3.17 $R_\odot$.

The effect of making the source surface non-spherical can be seen by comparing Figure 6, which is the ground-based eclipse photograph, with Figure 7. Figure 7a is based on a potential field model with a spherical source surface at r=2.72 $R_\odot$, which is the average radius of the non-spherical source surface used to construct Figures 5 and 7b. In Figures 7 and 8 starting points for tracing field lines have been chosen to emphasize the boundary field lines between open and closed structures. These field lines should lie immediately over helmet streamers and on the outer boundaries of coronal holes or other coronal structures. This choice is accomplished by starting to trace from a small distance on either side of polarity reversal contours of vanishing $\mathbf{B} \cdot \hat{n}$ on the source surface. Moreover, in order to emphasize the direction of the magnetic field lines beyond the source surface, each field line has been traced for 0.5 $R_\odot$ beyond the source surface. For a spherical source surface this extension is radial, but for non-spherical source surfaces it is along the local normal vector $\hat{n}$. Superimposed on these field lines are the field lines that start at the 400 locations on a grid of 18 x 36 points at

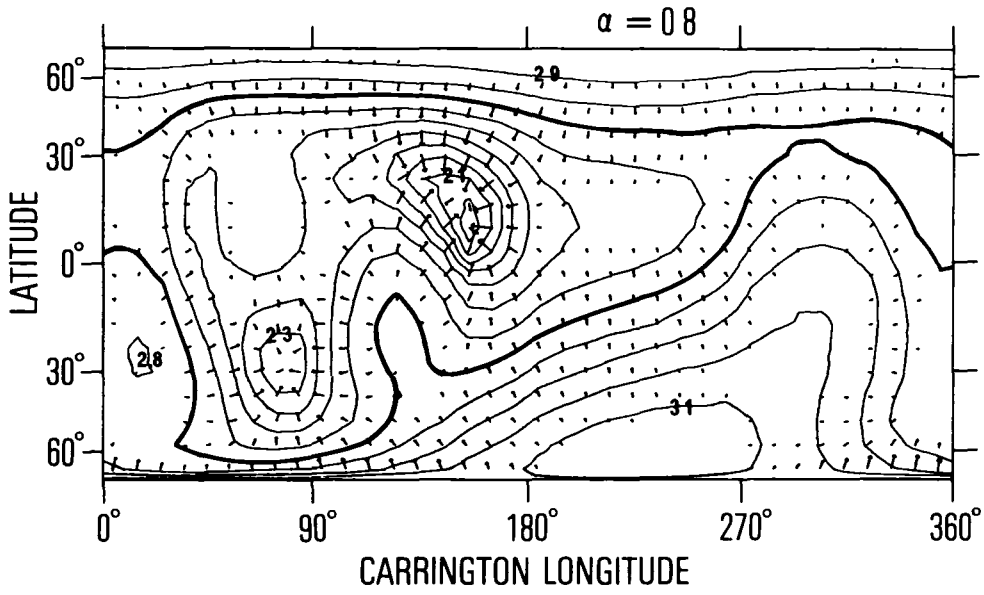

Figure 5 The source surface and unit normal vector for Carrington rotation 1602/3 (15 June 1973 to 12 July 1973). The format is the same as in Figure 4. The thickened contour line is $r_s = 2.72\ R_\odot$ ($\langle r_s \rangle = 2.7\ R_\odot$ for this case).

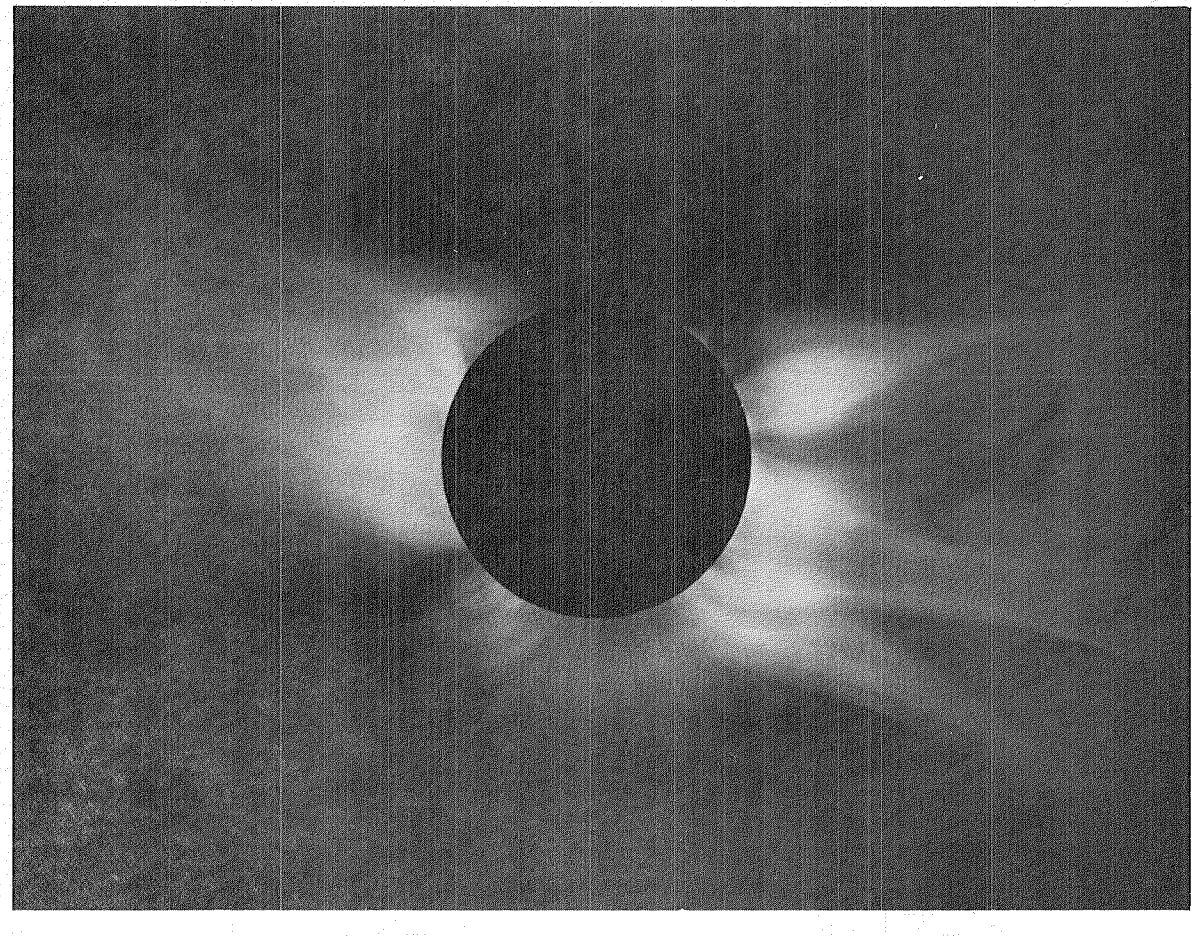

Figure 6 Photograph of the eclipse of 30 June 1973, courtesy of High Altitude Observatory.

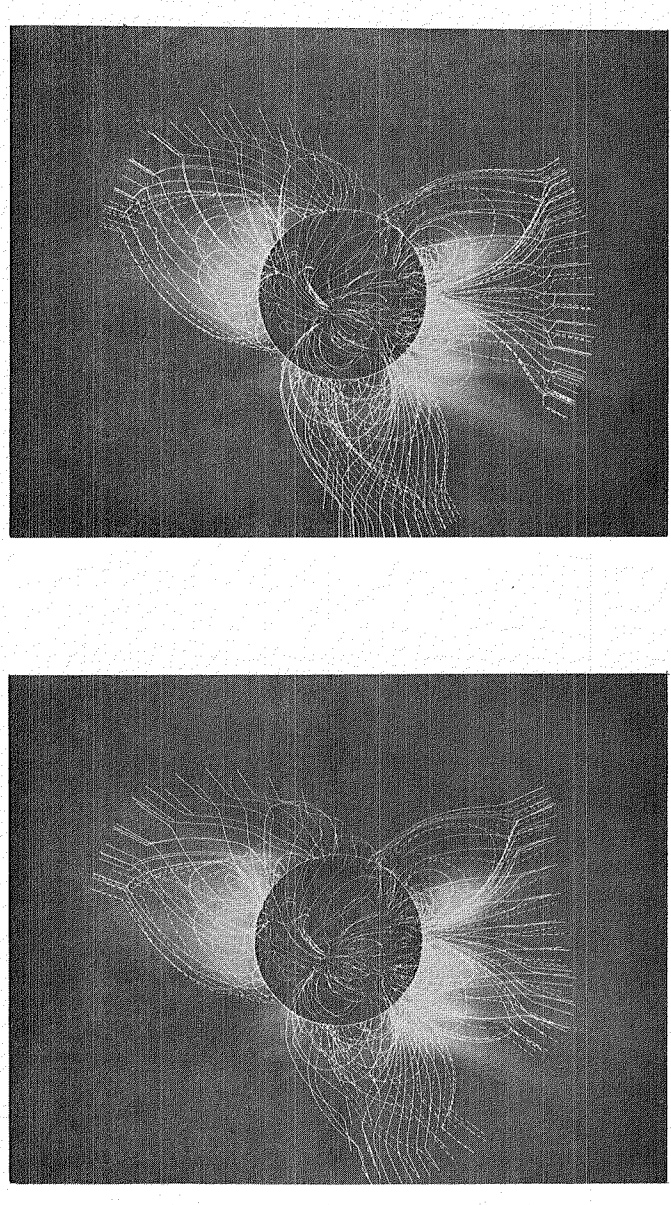

Figure 7 Comparison of calculated magnetic field lines with eclipse features. Top: α=0, *i*.e., the model with a spherical source surface. Bottom: α=0.8, *i*.e., the model with a non-spherical source surface. Dashed field lines lie behind the plane of the sky. See text for description of the algorithm for choosing which field lines to plot. North to the top, west to the right.

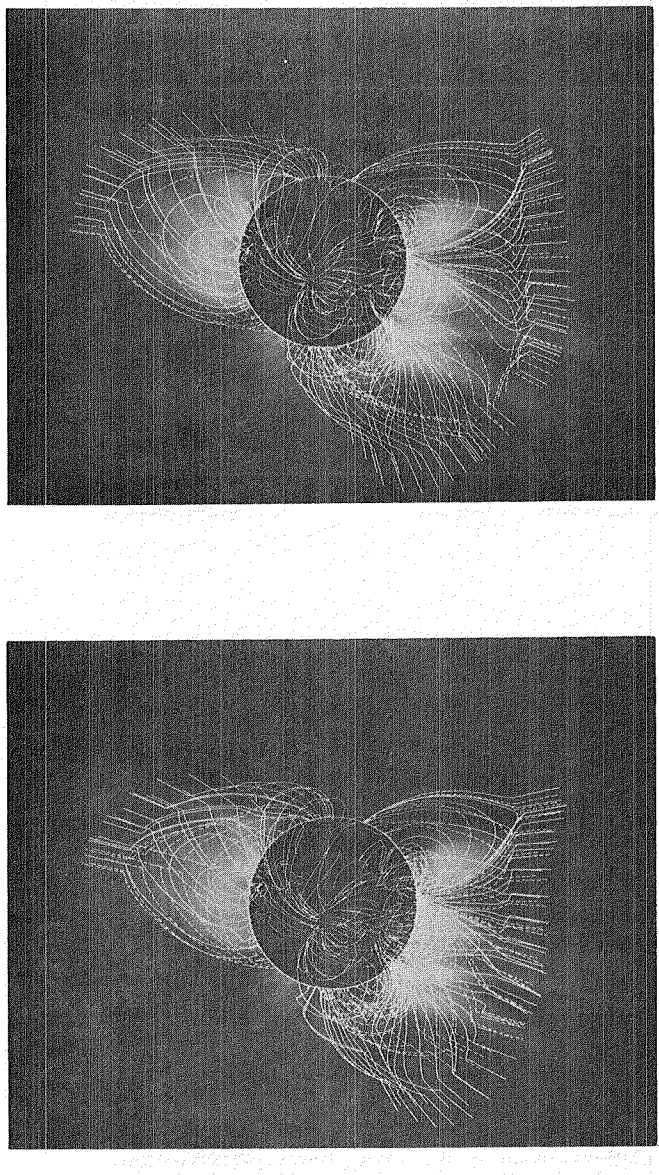

Figure 8 Identical in format to Figure 7 but with polar flux added, as described in the text.

$r=R_\odot$ which have the largest values of B_r. These field lines emphasize the closed structures that underlie the helmet streamers.

As expected, the primary difference between the two models is in the direction of the helmet streamers. Only a subtle difference in the corona, this will result in major differences in the predicted magnetic field strength throughout the heliosphere when the models are extended to $r \gtrsim 1$AU. A total of fifteen features have been identified extending beyond 2.5 $R_\odot$ on the eclipse photograph of Figure 6, and on the corresponding ATM coronagraph photograph (R. H. Munro, private communication, 1980). Features that extend radially outward from the spherical source surface (Figure 7a) correspond to similar features that extend normally outward from the non-spherical source surface (Figure 7b). For each feature the deviation from the radial direction was measured on the photograph and calculated from the direction of $\hat{n}$ at the source surface. The average equatorward deflection of the observed coronal streamers was 6.2°, with a rather large dispersion of 5.9°. The model streamers for a non-spherical source surface showed an equatorward deflection of 2.1° with a dispersion of 3.2°, indicating approximately a 30% improvement in this important aspect of coronal field modeling. Histograms of the equatorward deflections of the chosen features are shown in Figure 9.

In addition to the remaining 4.1° of equatorward deflection that the non-spherical source surface did not model, there are still other major discrepancies between the model and the observed coronal structure. The most glaring discrepancy is that the model has placed the large streamer in the southwest quadrant in the wrong location. It is calculated to be about 30° poleward of where it should be. This mislocation is far too great to be explained by a poor choice of the model parameters or by other inaccuracies of the model. Furthermore, the mislocation extends down to the very surface of the Sun, indicating that the source of the discrepancy lies with the input data. Because this particular

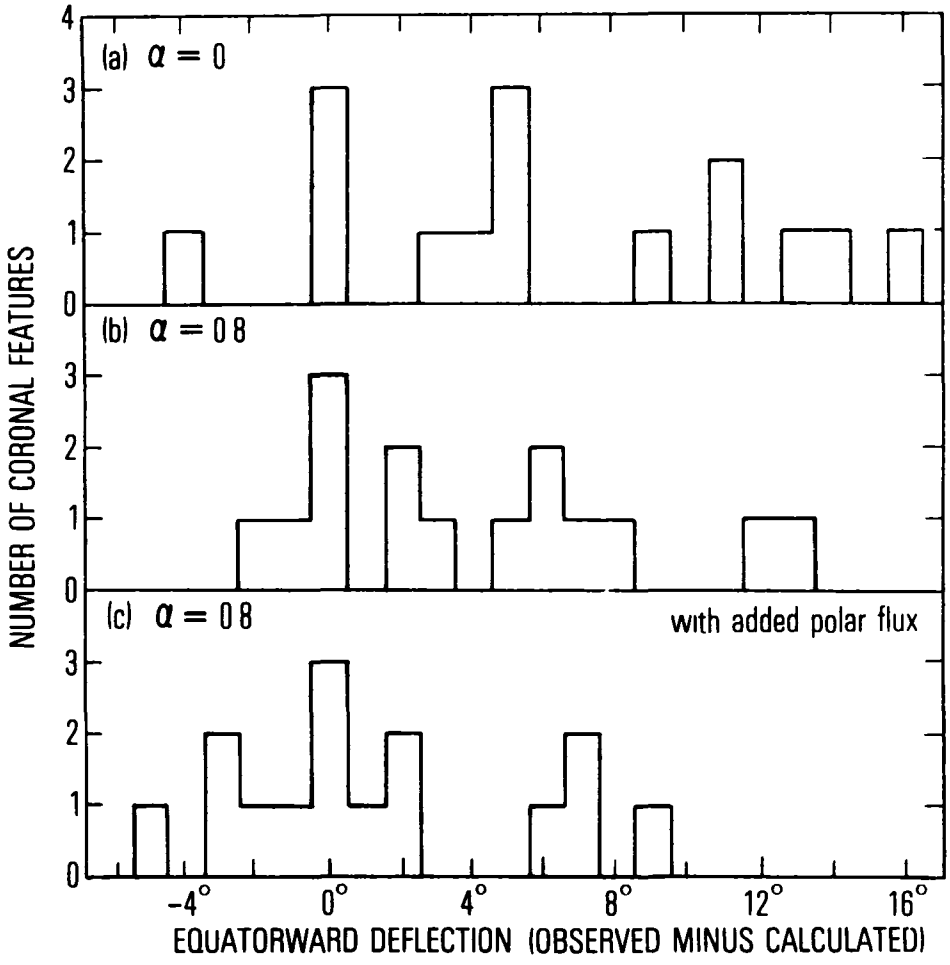

Figure 9 **Histograms of the differences (observed minus calculated) in the equatorward deflection of 15 coronal features observed outside the source surface: (a) Spherical source surface, *i.e.*, α=0; (b) Non-spherical source surface, α=0.8; (c) Non-spherical source surface, α=0.8, with added polar flux. Because the calculated equatorward deflection for the spherical source surface is zero, panel (a) is in fact a histogram of the observed deflections.**

streamer overlies a polar crown prominence, we suggest that the polar field strength has been underestimated by the magnetograph observations.

This is not a new hypothesis. It has been suggested by Pneuman *et al.* (1978) on the basis of similar data and reasoning. It has also been suggested by Suess *et al.* (1977) on the basis of coronal hole modeling, and by Svalgaard *et al.* (1978) on the basis of direct magnetograph data. The difficulties that magnetographs have when measuring polar fields has been a topic of extensive discussion for many years (*cf.* Howard, 1977, and references therein). In this latest case, we seem to have clear evidence (*i.e.*, the mislocation of a polar crown prominence) that the polar fields are indeed underestimated.

To test the hypothesis for this particular case, we have added polar magnetic flux to the magnetograph data and recomputed a new model (*i.e.*, a new source surface with the same $\langle r_s \rangle$ as before and new coefficients g_n^m, h_n^m, $\bar{g}_n^m$, $\bar{h}_n^m$). Polar flux has been added in accordance with the model proposed by Svalgaard *et al.* (1978). Specifically, poleward of 70° latitude we have added to the magnetograph data the radial magnetic field $\Delta B = \pm B_0 \hat{r} \cos^8\theta$, with B_0=11.56 G, the sign being chosen so as to reinforce the predominant polarities of the respective polar caps. We do not necessarily endorse this particular model nor imply that it is the only model that yields an acceptable fit with the coronal data. We have selected it because it is complete, recent, and based on magnetograph data only. There is probably a range of models for this "missing polar flux" that would produce similarly acceptable results.

Field line plots for the model with the added polar flux are shown in Figure 8. Figure 8a is based on a spherical source surface and Figure 8b on a non-spherical source surface (α=0.8) with the same added polar flux. As expected, the added polar flux has relocated and reoriented the helmet streamer in the southwest quadrant, in much better agreement with the observed streamer. Also, the average

equatorward deflection of all the chosen features is modeled much better with the added polar flux. The difference between observed and computed deflection is reduced from 4.1° without the added polar flux to 1.5° with added polar flux. The agreement is still not as good as one would like, but the present comparisons are sufficient to show that the addition of polar flux is necessary and sufficient to model polar crown streamers reasonably.

The large north polar coronal hole visible in Figures 6, 7, and 8 is the same hole that was studied extensively by Munro and Jackson (1977). A comparison can be made between the coronal hole boundaries measured by Munro and Jackson from coronagraph data, x-ray photographs, and K-coronameter data and the boundaries that would be inferred from the present models. This comparison is shown in Figure 10, where we have used the model that contains the added polar flux, *i.e.*, the model of Figure 8b. This model fits the observed boundary extremely well on the east limb, but the fit is poor on the west limb. The position of the predicted boundary is altered only slightly by making the source surface non-spherical rather than spherical, but the added polar flux improves the comparison greatly.

There are at least three factors which could contribute to an explanation of the discrepancy at the west limb. The first is the possibility that the photospheric magnetic field evolved significantly in the region underlying the west limb during the period between its central meridian passage and the eclipse (approximately one week). The second is the possibility that there may be closed magnetic structures in the corona which do not contain enough plasma to emit detectable amounts of visible or x-radiation. An example of such a situation would be the northern portion of the helmet structure on the northwest limb in Figure 8b. The third is the possibility that the polar regions may contain even more unobserved magnetic flux than proposed by Svalgaard *et al.* (1978). (The total additional polar cap flux in

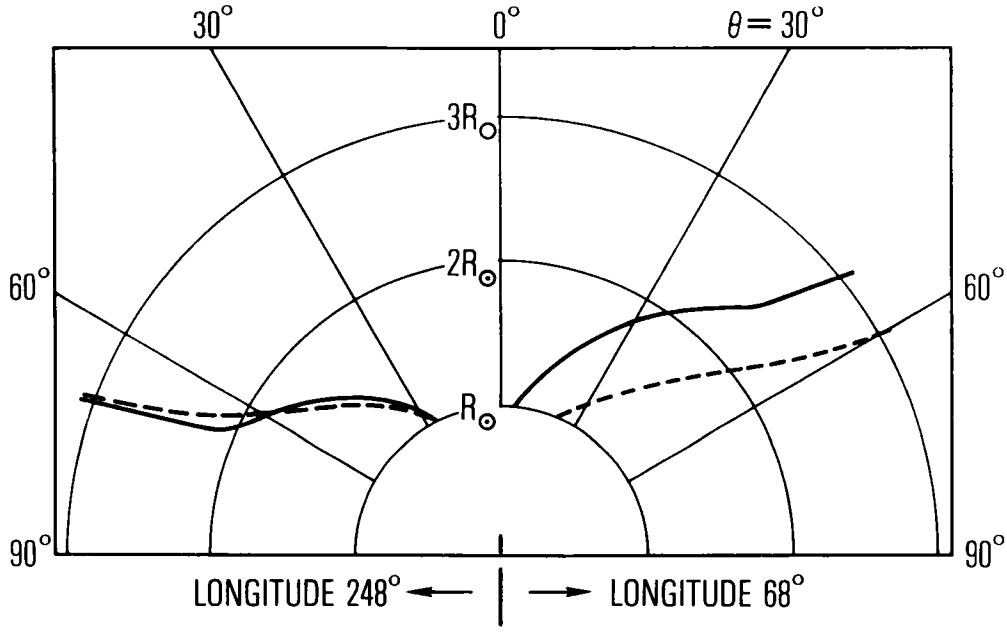

Figure 10 **Comparison of the boundary of the north polar coronal hole as predicted by the present model (solid lines) and as measured (dashed lines) by Munro and Jackson (1977).**

their model amounts to 3.24×10^{22}Mx.) The continued difference between the modeled and the observed streamer in the southwest quadrant argues in favor of this explanation.

An additional factor in the comparison of the model with coronal observations indicates an inherent limit to the applicability of potential field models themselves. The models of Figure 8 consistently calculate helmet streamers that are broader than observed. This is true in both equatorial and polar regions. A subsidiary result is that the calculated areas corresponding to the footpoints of open field lines are consistently smaller than the corresponding areas of observed coronal holes. This difference was studied by Levine (1977) using a spherical source surface, and it persists in the present work with non-spherical source surfaces. Because this difference is found at all latitudes, it cannot be ascribed to unobserved polar flux. It seems more likely that the observed helmet streamers are narrower than the calculated ones because there are current sheets at the boundaries between open and closed field lines, even inside the source surface. Such current sheets are, of course, not included in potential field models. One effect of such current sheets could be to make helmet streamers narrower than if the currents were not present. Physical reasons for expecting such current sheets are discussed in Section 6.

5. Magnetic Field Outside the Non-Spherical Source Surface

Our model magnetic field outside the source surface is given by a geometrical construction. In this construction we differ from Parker (1958) in detail, but not in spirit. Indeed, our basic principle is that solar wind plasma elements follow rectilinear trajectories upon emerging from the source surface. However, the trajectories are not radial because (a) the source surface is not spherical and (b) the source surface rotates with the sun. The geometrical construction requires us to transform between the non-rotating frame (in which the trajectories are rectilinear outside the source surface) and the co-rotating frame (in which the plasma elements flow parallel to B inside the source surface.

In the co-rotating frame the solar-wind velocity v is ideally normal to the source surface, as is B. (Within the source surface we have implemented this ideal only in the least-squares sense, but the procedure does not invalidate the ideal.) It follows that $\mathbf{v}=\hat{\mathbf{n}}\, v_n$. We assume for simplicity that v_n is constant over the source surface and adopt the value v_n=320 km/sec recommended by Hundhausen (1970). (One can permit v_n to be a function of latitude, but not longitude, if the source surface is azimuthally symmetric. In general, the permitted variation would be more subtle than this, and beyond the scope of the present work to describe. Interplanetary shocks result from the failure to impose appropriately restrictive conditions on the variation of v_n over the source surface.) It follows that the solar wind velocity in the non-rotating frame is given by

$$\mathbf{u} = \hat{\mathbf{n}}\, v_n + (\boldsymbol{\Omega} \times \mathbf{r})_s \,, \tag{9}$$

where $\boldsymbol{\Omega}$ is the angular velocity of the sun (corresponding to a siderial period $2\pi/\Omega \approx 25.1414$ days) and the subscript s denotes evaluation at the source surface.

It proves convenient to work in rectangular coordinates and to describe the trajectories parametrically by means of the time t after emission of the plasma

element from the source surface. We let the co-rotating system (x, y, z) coincide with the non-rotating system (x', y', z') at time t=0 (see Figure 11). The velocity of the plasma element in the non-rotating system is given by (9) as

$$u = (n_x v_n - \Omega y_s)\,\hat{x}' + (n_y v_n + \Omega x_s)\,\hat{y}' + n_z v_n \hat{z}' \tag{10}$$

at time t=0. We assume that the velocity remains constant for <u>all</u> t along the rectilinear trajectory. We assume further that $\underline{\Omega}$ is a constant vector parallel to $\hat{z}'$ *i.e.*, that differential rotation does not apply to large-scale magnetic fields. It follows from equation (10) that the trajectory of a plasma element is given parametrically by

$$x' = x_s + (n_x v_n - \Omega y_s)\,t \tag{11a}$$

$$y' = y_s + (n_y v_n + \Omega x_s)\,t \tag{11b}$$

$$z' = z_s + n_z v_n t \tag{11c}$$

for t>0, where $n_q \equiv (\hat{n} \cdot \hat{q})_s$. However, it follows from Figure 11 that

$$x' = x \cos \Omega t - y \sin \Omega t \tag{12a}$$

$$y' = x \sin \Omega t + y \cos \Omega t \tag{12b}$$

and z'=z. Substitution of (12) in (11) yields a pair of simultaneous linear equations for x and y, and it follows that

$$x = [x_s + (n_x v_n - \Omega y_s)t]\cos\Omega t + [y_s + (n_y v_n + \Omega x_s)t]\sin\Omega t \tag{13a}$$

$$y = [y_s + (n_y v_n + \Omega x_s)t]\cos\Omega t - [x_s + (n_x v_n - \Omega y_s)t]\sin\Omega t \tag{13b}$$

$$z = z_s + n_z v_n t \tag{13c}$$

along a plasma streamline in the co-rotating frame. Moreover, it follows from Parker's principle that (13) also constitutes the parametric equation of a field line outside the source surface.

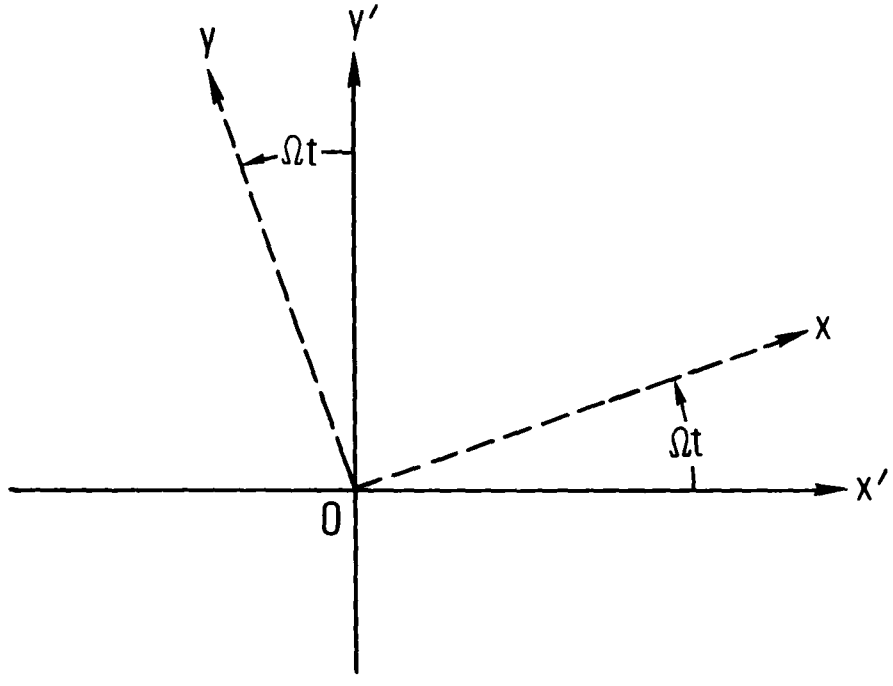

Figure 11 Relation between the rotating coordinate system (x, y, z) and the non-rotating coordinate system (x', y', z'). The z axis coincides with the z' axis and extends out of the plane of the paper.

While equation (13) can be used to trace any field line from the source surface to the outer boundary of the heliosphere, we use (13) in the present work to map the interplanetary current sheets associated with neutral lines on the source surface during June-July 1973. We use the photospheric data from rotations 1602 (last half) and 1603 (first half) with the added polar flux (as in Figure 8). There were two neutral lines (*i.e.*, contours of vanishing $\mathbf{B}\cdot\hat{\mathbf{n}}$) on the source surface during this (Skylab-eclipse) epoch. These are shown in synoptic-chart format in Figure 12a as solid curves. By means of equation (13) we have mapped these neutral lines from the source surface to heliocentric spheres of increasing radius. The loci of the current sheets at $r=10\,R_\odot$ and $r=50\,R_\odot$ are shown in Figure 12a as dashed and dotted curves, respectively. Figure 12b shows the locus of each current sheet at r=1AU (solid curves) and r=2AU (dashed curves). The displacement of these loci in longitude at interplanetary distances is a consequence of the spiral configuration of the magnetic field. The latitudinal displacement of current-sheet loci in the inner heliosphere ($r\lesssim 10\,R_\odot$) is a consequence of significantly non-radial flow of the solar wind there.

The polarity of the interplanetary magnetic field observed at r=1AU (King, 1975) is indicated on Figure 12b. It can be seen that two of the "sector boundary crossings" are very well modeled by our projection of the current sheets to 1AU, whereas the other two crossings are not well modeled. These latter crossings, however, are known to have enclosed a very high speed solar wind stream. We can see from this the need for properly modeling the variation of v_n over the source surface (rather than taking v_n as constant, as we have done for convenience in the present work). Moreover, the principal effect of a non-spherical source surface is on the latitudinal structure of the current sheet and comparison with observed ecliptic polarities is a limited test of the capabilities of the method.

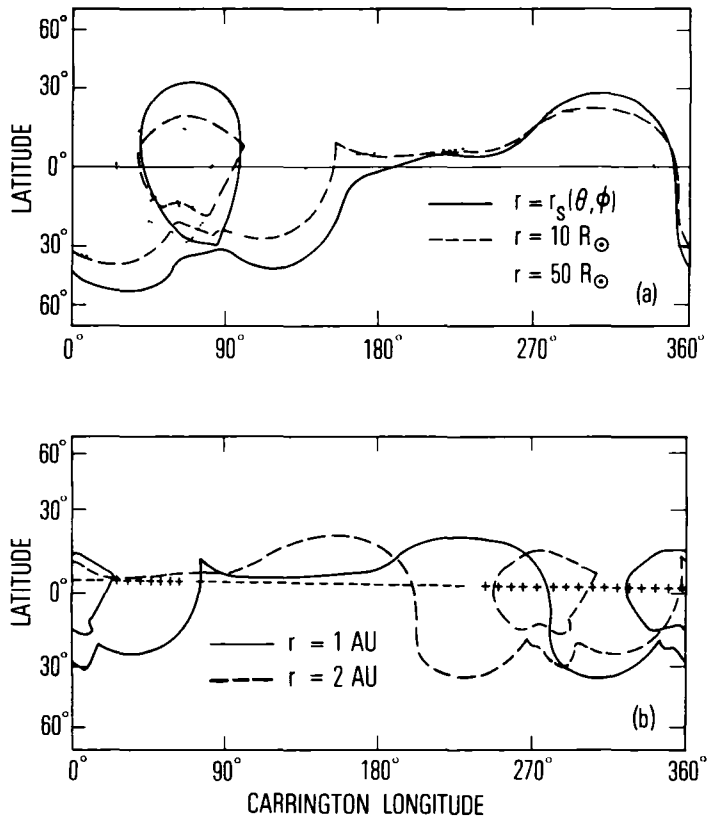

Figure 12 **Location of the interplanetary current sheets for Carrington rotation 1602/3 at different heliospheric distances in synoptic chart format. Panel (a): $r < 100\ R_\odot$. The latitudinal displacement of the current sheet results from the non-sphericity of the source surface and takes place mostly within $10\ R_\odot$. Panel (b): $r > 100\ R_\odot$. The longitudinal displacement perceptible in both panels results from the spiral configuration of the magnetic field. The measured polarity of the magnetic field at r=1AU in the ecliptic (King, 1975) is indicated in panel (b). This polarity should change sign upon traversal of the solid line.**

This Page Intentionally Left Blank

6. Summary and Discussion

We have developed the concept of the non-spherical source surface into a well-defined operational method for simulating the magnetic structure of the real solar corona and the real heliosphere. The method follows precedent by deriving the coronal **B** field inside the source surface from a scalar potential and the heliospheric **B** field outside the source surface from a geometrical construction. However, the non-spherical character of the source surface enables our method to simulate the non-radial orientation of helmet streamers and other characteristics of solar wind flow. We know from past analyses (Schulz, 1973; Schulz *et al.*, 1978) that some such recognition of the non-radial component of solar wind flow in the inner heliosphere is necessary in order to account for the observed magnitude of $|\mathbf{B}|$ in interplanetary space.

Our source surface is specified by equation (8) and contains an adjustable parameter α such that $0 \leq \alpha \leq 1$. The limit $\alpha=0$ corresponds to the spherical source surface of Altschuler and Newkirk (1969) and Schatten *et al.* (1969); the limit $\alpha=1$ corresponds to the non-spherical source surface of Schulz *et al.* (1978). The range $0.6 \leq \alpha \leq 0.8$ yields optimal agreement between our model and the full MHD solution of Pneuman and Kopp (1971) for the case of a photospheric dipole. It is our working hypothesis that the same range of α (*i.e.*, $\alpha \approx 0.6$-0.8) is appropriate to the study of the real corona also.

Using photospheric magnetograph data centered on the Skylab-era eclipse of 30 June 1973, we have found that our present method adequately models the non-radial orientation of helmet streamers in eclipse and coronagraph photographs if additional magnetic flux is superimposed on the polar regions. However, observed helmet streamers are consistently narrower in latitude than those calculated by our method, and observed coronal holes are often larger in area (*cf.* Levine, 1977) than the footpoint regions of open field lines calculated by our method. These

discrepancies are tentatively attributed to the neglect of coronal current sheets that are likely to occur (even at $r<r_s$) at the boundary between closed and open field lines in consequence of the discontinuity in plasma pressure. It is known, after all, that coronal holes correspond to regions of lower plasma density and temperature than the coronal arcades that form helmet streamers (*e.g.*, Bohlin, 1977). Thus, the discrepancies between observed and calculated coronal hole areas and helmet streamer widths may well be intrinsic to our model, as well as to other models in which **B** is derived from a scalar potential within the source surface.

Although mathematical difficulties prevent us from enforcing the desired boundary condition $|\mathbf{B} \times \hat{\mathbf{n}}|=0$ at every point on the source surface, our procedure of minimizing the mean value of $|\mathbf{B} \times \hat{\mathbf{n}}|^2$ proves to be quite successful. Field-line plots (*e.g.*, Figure 3) show that $\hat{\mathbf{B}}$ is nearly perpendicular to the source surface everywhere except near the neutral lines from which interplanetary current sheets (*e.g.*, Figure 12) originate. However, the derivation of **B** from a scalar potential in the corona necessarily causes neutral lines on the source surface to be Y-type rather than cusp-type (Sturrock and Smith, 1968; Pneuman and Kopp, 1971). Thus, one could not expect the last closed coronal field line to be perpendicular to the source surface there, even to a spherical source surface. Our field-line plots (Figures 3, 7, and 8) show that the least-squares method yields a <u>very</u> good approximation to the ideal of a Y-type neutral line on the source surface.

In summary, our implementation of the non-spherical source surface and least-squares method of imposing the coronal boundary condition there yield results that agree quite well with observation upon adjustment of only a few parameters. Further applications of the method to real and idealized solar conditions immediately suggest themselves and will be treated in future works of more specialized scope. We conclude, on the basis of results obtained so far, that the use of a non-

spherical source surface constitutes a significant procedural advancement in the modeling of coronal and heliospheric magnetic fields.

This Page Intentionally Left Blank

Appendix: Mathematical Detail

We have deliberately kept the equations simple in the main text. For those readers who need or would prefer a mathematically explicit description of our procedures, we offer this Appendix.

We assume that the scalar magnetic potential is given formally by equation (1) for $R_O \le r \le r_s(\theta,\phi)$, but we recognize that the coefficients $(\bar{g}_n^m, \bar{h}_n^m)$ and (g_n^m, h_n^m) are related as in equation (2) only for the special case of a spherical source surface. For the more general case of a non-spherical source surface we must differentiate σ (*cf.* equation (5)) with respect to each of the $\bar{g}_{n'}^{m'}$ and each of the $\bar{h}_{n'}^{m'}$ in order to minimize σ. We require specifically that

$$\frac{\partial\sigma}{\partial\bar{g}_{n'}^{m'}} = 2\int [\mathbf{B}\cdot\frac{\partial\mathbf{B}}{\partial\bar{g}_{n'}^{m'}} - (\hat{\mathbf{n}}\cdot\mathbf{B})\,\hat{\mathbf{n}}\cdot\frac{\partial\mathbf{B}}{\partial\bar{g}_{n'}^{m'}}]\,dA = 0 \qquad \text{(A1a)}$$

and

$$\frac{\partial\sigma}{\partial\bar{h}_{n'}^{m'}} = 2\int [\mathbf{B}\cdot\frac{\partial\mathbf{B}}{\partial\bar{h}_{n'}^{m'}} - (\hat{\mathbf{n}}\cdot\mathbf{B})\,\hat{\mathbf{n}}\cdot\frac{\partial\mathbf{B}}{\partial\bar{h}_{n'}^{m'}}]\,dA = 0\,, \qquad \text{(A1b)}$$

where $dA = r^2\,|\hat{\mathbf{n}}\cdot\hat{\mathbf{r}}|^{-1}\,d(\cos\theta)\,d\phi$ is the element of area on the source surface. Unless $|\hat{\mathbf{n}}\cdot\hat{\mathbf{r}}|$ is zero at some point on the source surface the area element dA is well defined. We intend to avoid such pathological cases, for both physical and mathematical reasons. We can make subsequent steps in the derivation of the $(\bar{g}_n^m, \bar{h}_n^m)$ more compact by writing $\mathbf{B}\equiv\tilde{\mathbf{B}} + \bar{\mathbf{B}}$, with $\tilde{\mathbf{B}}$ given by equation (7) and $\bar{\mathbf{B}}$ given by

$$\bar{\mathbf{B}} = -R_O\,\nabla \sum_{n=1}^{\bar{N}}\sum_{m=0}^{n} \left(\frac{r}{R_O}\right)^n (\bar{g}_n^m \cos m\phi + \bar{h}_n^m \sin m\phi)\, P_n^m(\theta)\,, \qquad \text{(A2)}$$

because we know that $\partial\tilde{\mathbf{B}}/\partial\bar{g}_{n'}^{m'} = \partial\tilde{\mathbf{B}}/\partial\bar{h}_{n'}^{m'} = 0$. Thus, it follows from (A1) that

$$\int [\bar{\mathbf{B}}\cdot\frac{\partial\bar{\mathbf{B}}}{\partial\bar{g}_{n'}^{m'}} - (\hat{\mathbf{n}}\cdot\bar{\mathbf{B}})\,\hat{\mathbf{n}}\cdot\frac{\partial\bar{\mathbf{B}}}{\partial\bar{g}_{n'}^{m'}}]\,dA$$

$$= \int [(\hat{n} \cdot \tilde{B})\, \hat{n} \cdot \frac{\partial \bar{B}}{\partial \bar{g}_{n'}^{m'T}} - \tilde{B} \cdot \frac{\partial \bar{B}}{\partial \bar{g}_{n'}^{m'T}}]\, dA \qquad \text{(A3a)}$$

and

$$\int [\bar{B} \cdot \frac{\partial \bar{B}}{\partial \bar{h}_{n'}^{m'T}} - (\hat{n} \cdot \bar{B})\, \hat{n} \cdot \frac{\partial \bar{B}}{\partial \bar{h}_{n'}^{m'T}}]\, dA$$

$$= \int [(\hat{n} \cdot \tilde{B})\, \hat{n} \cdot \frac{\partial \bar{B}}{\partial \bar{h}_{n'}^{m'T}} - \tilde{B} \cdot \frac{\partial \bar{B}}{\partial \bar{h}_{n'}^{m'T}}]\, dA \qquad \text{(A3b)}$$

for each n' (=1, 2, 3,. . ., $\bar{N}$) and m' (=0, 1, 2,. . ., n). We observe that

$$\frac{\partial \bar{B}}{\partial \bar{g}_{n'}^{m'T}} = -R_0 \nabla [\left(\frac{r}{R_0}\right)^{n'} P_{n'}^{m'}(\theta) \cos m'\phi] \qquad \text{(A4a)}$$

and

$$\frac{\partial \bar{B}}{\partial \bar{h}_{n'}^{m'T}} = -R_0 \nabla [\left(\frac{r}{R_0}\right)^{n'} P_{n'}^{m'}(\theta) \sin m'\phi]\,, \qquad \text{(A4b)}$$

i.e., that both are independent of the expansion coefficients ($\bar{g}_{n'}^{m'}$, $\bar{h}_{n'}^{m'}$). Thus, it follows that (A3) constitutes a set of $\bar{N}^2+2\bar{N}$ simultaneous linear algebraic equations for the ($\bar{g}_n^m$, $\bar{h}_n^m$). A more explicit representation of (A3a) is given in equation (6). Equation (6) thus formally represents $\frac{1}{2}\bar{N}(\bar{N}+3)$ separate linear equations for the $\bar{N}^2+2\bar{N}$ unknown parameters ($\bar{g}_n^m$, $\bar{h}_n^m$). The other $\frac{1}{2}\bar{N}(\bar{N}+1)$ required equations are obtained by replacing $\cos m'\phi$ with $\sin m'\phi$ ($m' \neq 0$) in equation (6) at each of the eight places where $\cos m'\phi$ appears.

The orthogonality properties of the harmonic functions reduce equation (6) and its complement to equation (2) for the case of a spherical source surface, *i.e.*, for

$r=R_0$ and $\hat{n}=\hat{r}$. The more general and interesting case of a non-spherical source surface finds $r=r_s(\theta,\phi)$ and $\hat{n}\neq\hat{r}$ in (6). The orthogonality properties of the harmonic functions are no longer useful, because the integrand now contains vastly more complicated functions of θ and ϕ as well. However, we can express (6) and its complement in matrix form by ordering the coefficients $(\bar{g}_n^m, \bar{h}_n^m)$ into an $(\bar{N}^2+2\bar{N})$-component vector C_s as follows:

$$(C_1, C_2, C_3, \ldots, C_{\bar{N}^2+2\bar{N}})$$

$$= (\bar{g}_1^0, \bar{g}_1^1, \bar{h}_1^1, \bar{g}_2^0, \bar{g}_2^1, \bar{g}_2^2, \bar{h}_2^1, \bar{h}_2^2, \bar{g}_3^0, \ldots, \bar{h}_{\bar{N}}^{\bar{N}}) \qquad \text{(A5)}$$

Thus, priority in the sequence goes first to the smaller values of n over the larger, then to g over h, and finally to the smaller values of m over the larger. Similarly, the right-hand side of equation (6) and its complement, on which n" and m" are dummy variables only, can be ordered into an $(\bar{N}^2+2\bar{N})$-component vector K_p by giving priority first to the smaller values of n' over the larger, then to equation (6) over its complement containing $\sin m'\phi$ instead of $\cos m'\phi$, and finally to the smaller values of m' over the larger. With this ordering convention (or any other that is internally consistent) we can reduce equation (6) and its complement to the form

$$\sum_{s=1}^{\bar{N}^2+2\bar{N}} \Lambda_{ps} C_s = K_p , \qquad \text{(A6)}$$

in which the elements of the Λ matrix are the integrals that appear as coefficients of $\bar{g}_n^m$ and $\bar{h}_n^m$ on the left-hand side of (6) and its complement. The matrix elements Λ_{ps} must (of course) be arrayed in accordance with the convention chosen for ordering the vector components K_p and C_s. By solving (A6) we obtain the set of expansion coefficients $(\bar{g}_n^m, \bar{h}_n^m)$ in (1) that will minimize the mean-square tangential component of B over the source surface. This completes our basic objective.

It is important to ascertain whether the coefficients $(\bar{g}_n^m, \bar{h}_n^m)$ thus determined are truly accurate for the case considered and reasonably stable against minor changes in $\bar{N}$, in the (g_n^m, h_n^m), or in the parameter α in equation (8), for example. Thus, it is encouraging to know that our numerical code yields results in agreement with equation (2) for α=0, in agreement with expectations dictated by symmetry (see Section 3) in the case of a photospheric dipole for general α, and in agreement (see Section 4) with the numerical results of Schulz *et al.* (1978) for the special case of a photospheric dipole with α=1. When we obtain the coefficients $(\bar{g}_n^m, \bar{h}_n^m)$ from real magnetic data rather than from an idealized model of the photospheric B field, then (of course) there is no standard set of coefficients $(\bar{g}_n^m, \bar{h}_n^m)$ against which to compare those calculated by minimizing σ over a non-spherical source surface. Indeed, standard sets of coefficients $(\bar{g}_n^m, \bar{h}_n^m)$ are available only for the simplest of idealized models (Schulz *et al.*, 1978). However the stability of coefficients $(\bar{g}_n^m, \bar{h}_n^m)$ determined numerically by minimizing σ, either in a realistic case or in an idealization more complex than the photospheric dipole case, can be judged by an inspection of the $\mathbf{A}$ matrix that appears in (A6) and whose elements are the integrals that appear as coefficients of the unknown quantities $(\bar{g}_n^m, \bar{h}_n^m)$ on the left-hand side of equation (6) and its complement. For the $(\bar{g}_n^m, \bar{h}_n^m)$ determined by solving these linear equations to be stable against small changes in $r_s(\theta,\phi)$ or $\bar{N}$, the matrix $(\mathbf{A})$ of the coefficients must be well-conditioned, *i.e.*, free of eigenvalues that either vanish or are too small because of a failure (or near-failure) of the rows of $\mathbf{A}$ to be linearly independent of each other. Our experience suggests that we have little to fear in this regard. While the $\mathbf{A}$ matrix is strictly diagonal only in the limit of a spherical source surface (α=0), it is nearly diagonal in the other cases that we have examined. In other words, the elements A_{ps} in (A6) become progressively and substantially smaller in magnitude as one steps away from the main diagonal (p=s). This property is generally sufficient to assure that a matrix is well-conditioned. Moreover, we have

encountered no obvious difficulties in seeking solutions of (A6). The solutions for the $(\bar{g}_n^m, \bar{h}_n^m)$ seem to vary continuously with α, for example (see Figure 3), and weakly with $\bar{N}$. Thus, we find overall that our method is well-behaved, and we have full confidence in it.

Having thus obtained the optimal coefficients $(\bar{g}_n^m, \bar{h}_n^m)$ for use in (1), we can proceed to plot field lines inside the source surface, *i.e.*, for $R_\odot \le r \le r_s(\theta,\phi)$. This is easy enough to do, starting either from a footpoint at $r=R_\odot$ or from a point on the source surface, because the trajectory of a field line is defined locally by the direction of **B**. Having obtained the coefficients (g_n^m, h_n^m) and $(\bar{g}_n^m, \bar{h}_n^m)$, we calculate the components (B_r, B_θ, B_ϕ) of $\mathbf{B}=-\nabla V$ from (3). As usual the field line must satisfy the equations

$$\frac{dr}{ds} = \frac{B_r}{B} \quad , \quad r\left(\frac{d\theta}{ds}\right) = \frac{B_\theta}{B} \quad , \quad r\sin\theta\left(\frac{d\phi}{ds}\right) = \frac{B_\phi}{B} , \tag{A7}$$

where $B=|\mathbf{B}|$ and ds is the element of arc length along the trajectory. We use a Runge-Kutta method to be certain that the computed trajectory truly tracks the field line (despite the finite step size). Outside the source surface we plot field lines with the aid of (13), thus imposing a boundary condition that **B** is exactly normal to the source surface. In other words, we do <u>not</u> "continue" the direction of the numerically computed magnetic field across the source surface from inside to outside, because there might be a significant error locally in doing so (despite the global minimization of σ). Thus, the footpoint of the interplanetary segment of a field line coincides with the point at which the coronal segment of the same field line touches the source surface from the inside. We accept the small discontinuity in $\hat{\mathbf{n}} \times \mathbf{B}$ that is inevitable in such a construction when the source surface is non-spherical, but we would assume the continuity of $\hat{\mathbf{n}} \cdot \mathbf{B}$ across the source surface in order to calculate the magnitude of $|\mathbf{B}|$ in interplanetary space (Schulz *et al.*, 1978). The actual calculation of $|\mathbf{B}|$ along a field line outside the source surface

involves numerical application of differential geometry and is not yet completed. Thus, we have been content in the present work to obtain the direction of B from the fact that

$$\hat{B} = \pm \frac{(\dot{x}\,\hat{x} + \dot{y}\,\hat{y} + \dot{z}\,\hat{z})}{(\dot{x}^2 + \dot{y}^2 + \dot{z}^2)^{1/2}} \tag{A8}$$

and to trace the field lines themselves by means of equation (13). Field lines would be rectilinear outside the source surface except for the garden-hose effect caused by the rotation of the sun (Parker, 1958). Indeed, at heliocentric distances $r \lesssim 10\,R_\odot$ the field lines described by equation (13) deviate negligibly from rectilinear projections of the outward normals $\hat{n}$ from the various points on the source surface, and we have used this fact to simplify the computations underlying Figures 3, 7, and 8. However, the spiral configuration of B is very important at interplanetary distances, as is well known. Thus, it has been absolutely essential to use equation (13) in its full generality for the purpose of locating the interplanetary current sheets in Figure 12 (especially so in Figure 12b).

References

Adams, J. and Pneuman, G.W.: 1976, *Solar Phys.*, **46**, 185.

Altschuler, M.D. and Newkirk, G., Jr.: 1969, *Solar Phys.*, **9**, 131.

Altschuler, M.D., Levine, R.H., Stix, M. and Harvey, J.W.: 1976, *Solar Phys.*, **51**, 345.

Bohlin, J.D.: 1977, in J.B. Zirker (ed.), *Coronal Holes and High Speed Solar Wind Streams*, Colo. Assoc. Univ. Press, Boulder, pp. 27-69.

Burlaga, L.F., Behannon, K.H., Hansen, S.F. and Pneuman, G.W.: 1978, *J. Geophys. Res.*, **83**, 4177.

Howard, R.: 1977, *Ann. Rev. Astron. Astrophys.*, **15**, 153.

Hundhausen, A.: 1970, *Rev. Geophys. Space Phys.*, **8**, 729.

Jackson, B.V. and Levine, R.H.: 1980, *Solar Phys.*, in press.

King, J.H. (ed.): 1975, *Interplanetary Magnetic Field Data*, World Data Center A for Solar-Terrestrial Physics Report UAG-46, NOAA, Boulder, Colo.

Levine, R.H.: 1977, *Astrophys. J.*, **218**, 291.

Levine, R.H.: 1978, *J. Geophys. Res.*, **83**, 4193.

Levine, R.H. and Altschuler, M.D.: 1974, *Solar Phys.*, **36**, 345.

Levine, R.H., Altschuler, M.D. and Harvey, J.W.: 1977, *J. Geophys. Res.*, **82**, 1061.

Munro, R. and Jackson, B.V.: 1977, *Astrophys. J.*, **213**, 874.

Nerney, S.F. and Suess, S.T.: 1975, *Astrophys. J.*, **196**, 837.

Parker, E.N.: 1958, *Astrophys. J.*, **128**, 664.

Pneuman, G.W. and Kopp, R.A.: 1971, *Solar Phys.*, **18**, 258.

Poletto, G., Vaiana, G.S., Zombeck, M.V., Krieger, A.S., and Timothy, A.F.: 1975, *Solar Phys.*, **44**, 83.

Riesebieter, W. and Neubauer, F.M.: 1979, *Solar Phys.*, **63**, 127.

Schatten, K.H.: 1968, *Nature*, **220**, 1211.

Schatten, K.H., Wilcox, J.M. and Ness, N.F.: 1969, *Solar Phys.*, **9**, 442.

Schulz, M.: 1973, *Astrophys. Space Sci.*, **24**, 371.

Schulz, M., Frazier, E.N. and Boucher, D.J., Jr.: 1978, *Solar Phys.*, **60**, 83.

Smerd, S.F. and Dulk, G.A.: 1971, in R. Howard (ed.), *IAU Symposium No. 43, Solar Magnetic Fields*, Reidel, Dordrecht-Holland, pp. 616-641.

Smith, S. and Schatten, K.H.: 1970, *Nature*, **226**, 1130.

Sturrock, P.A. and Smith, S.M.: 1968, *Solar Phys.*, **5**, 87.

Suess, S.T., Richter, A.K., Winge, C.R. and Nerney, S.F.: 1977, *Astrophys. J.*, **217**, 296.

Svalgaard, L., Duvall, T.L., Jr., and Scherrer, P.H.: 1978, *Solar Phys.*, **58**, 225.

Svestka, Z., Solodyna, C.V., Howard, R. and Levine, R.H.: 1977, *Solar Phys.*, **55**, 359.

Uchida, Y., Altschuler, M.D. and Newkirk, G.A., Jr.: 1973, *Solar Phys.*, **28**, 495.

End of Document